aerospace

MDPI

Article

Study on the Influence of Medium Temperature on the Performance of a Space Micropump

Danyang Zhou, Jintao Liu *, Lilei Miao, Zhen Qu, Kaiyun Gu and Zhanhai Zhang

Beijing Institute of Control Engineering, Beijing 100094, China; zhoudanyang02@126.com (D.Z.); miaoxinyu@163.com (L.M.); quzhen@buaa.edu.cn (Z.Q.); kaiyungu@163.com (K.G.); 18210591069@163.com (Z.Z.)
* Correspondence: ljt86@zju.edu.cn

Abstract

The present work examines how variations in working fluid temperature govern the hydrodynamic behavior of a space-rated micropump. Using perfluorotriethylamine as the operating medium, three-dimensional CFD simulations employing the SST k-ω turbulence closure were carried out across a broad thermal spectrum, and the resulting flow physics were interpreted through entropy generation analysis. Based on the entropy production theory, the influence laws of different inlet temperatures on the external characteristics, internal characteristics, and flow loss characteristics of the micropump were quantitatively analyzed. The results show that temperature mainly affects the micropump performance by changing the viscosity and density of the working fluid. At low temperatures, the fluid viscosity increases significantly, leading to increased flow resistance, intensified internal friction, reduced head and efficiency, and increased shaft power. As the temperature increases to 0 °C and above, the viscosity change tends to moderate, and the external characteristic parameters tend to stabilize. The internal characteristic analysis shows that under low-temperature conditions, the high-pressure region in the impeller area expands and the turbulent kinetic energy decreases, but the flow separation is to a certain extent suppressed. The region near the volute tongue and the impeller outer edge are the main areas of entropy production loss, and their entropy production rates increase significantly with decreasing temperature. Moreover, at low temperatures, the high entropy production regions expand from locally isolated distributions to continuous large-scale distributions. The impeller outer edge dominates total entropy production, driven by peak fluid linear velocity and intense shear interaction with the volute wall. The findings elucidate how working fluid temperature governs both the hydrodynamic performance and the irreversible loss characteristics of the micropump. These insights can directly inform the engineering design of thermal management loops intended for orbital applications under severe temperature swings.

Keywords: space micropump; temperature effect; entropy production; flow characteristics

Check for updates

Academic Editor: Kyun Ho Lee

Received: 9 June 2026
Revised: 24 July 2026
Accepted: 25 July 2026
Published: 28 July 2026

Copyright: © 2026 by the authors. Licensee MDPI, Basel, Switzerland. This article is an open access article distributed under the terms and conditions of the Creative Commons Attribution (CC BY) license.

1. Introduction

In modern spacecraft, payloads are being consolidated into higher-density packages with expanding functional requirements. Sustained operation under these conditions produces concentrated thermal loads that must be actively managed to prevent component degradation or mission-critical failures [1]. Mechanically pumped fluid loops have emerged as the baseline thermal architecture for such high-power platforms, owing to their mechanical simplicity and demonstrated robustness in long-duration flight applications [2,3]. A

space-qualified micropump drives the coolant through these loops, extracting waste heat from avionics and payloads and rejecting it via radiators, thereby maintaining equipment within allowable temperature margins across the full orbital thermal cycle [4].

Serving as the prime mover in pumped fluid loops, the micropump must deliver stable hydraulic performance across the extreme temperature range encountered in orbit. Established working fluids for such applications include perfluorotriethylamine, liquid ammonia, and other specialty refrigerants [5,6]. The thermophysical properties of these media—density, viscosity, saturated vapor pressure—exhibit significant thermal sensitivity, which in turn alters the internal flow topology, pressure field, and dissipation characteristics of the pump [7–10]. Consequently, resolving how medium temperature couples with the pump's hydrodynamic and loss behavior is essential for ensuring reliable operation of spacecraft active thermal management in flight.

In recent years, domestic and international scholars have conducted extensive research on the internal flow characteristics of centrifugal pumps [11]. In terms of numerical simulation methods, computational fluid dynamics (CFD) technology has become an important tool for studying complex flow phenomena inside pumps [12]. Rakibuzzaman et al. [13] conducted numerical and experimental investigations of cavitation flows in a multistage centrifugal pump, verifying the accuracy of CFD methods for predicting cavitation behavior. Dehghan et al. [14] explored a new criterion to determine the onset of cavitation in centrifugal pumps from an energy-saving standpoint through experimental and numerical investigation. In terms of turbulence model selection, the SST k-ω turbulence model has been widely applied in internal flow simulations of pumps due to its good performance in both near-wall and far-field regions.

Various degradation mechanisms affecting centrifugal pump operation, 59 cavitation stands out as a particularly detrimental phenomenon that has received sustained 60 research attention. Fundamental theory and simulation methods were provided by Franc and Michel [7]. Ge et al. [9] highlighted temperature effects on bubble dynamics, while Coutier-Delgosha et al. [12] clarified cavitation's impact on performance. Tao et al. [15] studied pump turbine cavitation, and Zhang et al. [16] demonstrated that splitter blades improve resistance.

The strong thermal sensitivity of pump performance has motivated extensive research on temperature dependent phenomena in turbomachinery. Early efforts explored cavitation behavior in various fluids, thermodynamic effects using B factor theory, similarity laws, and prediction methods for cavitation at different temperatures [17–22]. Subsequent visualization and experiments on inducers [23–26] revealed thermal influences on leading edge cavitation and instabilities. More recently, predictive models incorporating thermodynamic effects were developed for centrifugal pumps [27,28], and two phase flow in spacecraft evaporators was also investigated [29].

The second-law framework—specifically entropy generation analysis—has gained traction as a diagnostic tool for identifying and quantifying irreversible dissipation in pump flow fields. Qi et al. [30] conducted performance optimization research on centrifugal pumps based on the particle swarm optimization algorithm and entropy production theory, finding that the impeller and volute are the two regions with the largest entropy production. Shi et al. [31] applied the entropy production theory to analyze the energy loss characteristics in the stall region of a tubular pump, revealing the influence mechanism of gap backflow on flow losses. Gong et al. [32] applied the entropy production analysis method to the energy loss research of turbines, demonstrating the advantages of this method in determining the location and magnitude of energy dissipation. Entropy production analysis can distinguish between turbulent entropy production and wall entropy production, providing an effective means for identifying the main sources of flow losses.

In terms of spacecraft thermal control system applications, mechanically pumped fluid loop technology has achieved significant progress. Bhandari et al. [33] provided a detailed introduction to the application history and development status of mechanically pumped fluid loops in spacecraft thermal control. Birur et al. [34] investigated the application prospects of MEMS-based micropump cooling systems in micro/nano spacecraft.

Although internal flows, thermodynamic effects, and loss mechanisms in conventional centrifugal pumps are well documented, space micropumps using specialty fluids over wide thermal ranges remain under-explored. In particular, the coupled response of the internal flow topology, dissipation distribution, and hydrodynamic stability to systematically varied medium temperature has yet to be fully resolved. The present work addresses this gap through a parametric CFD investigation spanning six inlet temperatures (−37 °C to 72 °C), employing entropy production diagnostics to decompose and attribute the resulting flow losses. By correlating external performance metrics (head, shaft power, efficiency) with detailed internal field data, the analysis clarifies the physical pathways through which medium temperature governs micropump behavior, thereby informing the robust design of next-generation spacecraft thermal control loops.

2. Computational Model

The computational domain encompassed the full three-dimensional geometry of a miniature centrifugal pump, discretized with structured hexahedral grids. External performance maps (head, shaft power, efficiency versus flow rate) were generated through steady-state simulations at six uniformly spaced inlet temperatures spanning −37 °C to 72 °C, with a fixed inlet static pressure of 0.2 MPa, with a mass flow outlet boundary condition, a rotational speed of 8000 rpm, adiabatic wall thermal conditions, and a Multiple Reference Frame (MRF) approach for the rotating/stationary interfaces. Convergence was strictly judged by RMS residuals dropping below 10^{-8}. At the rated flow point, cross-sectional fields of pressure, velocity, and turbulent kinetic energy were extracted for each thermal condition to resolve the temperature-dependent evolution of the flow topology. Entropy production rates were computed across all solid boundaries and the fluid volume to enable a spatially resolved loss audit.

Under the simulated operating conditions, cavitation and phase change do not occur. The chosen inlet static pressure of 0.2 MPa, combined with the pressure rise generated by the pump, ensures that the local static pressure throughout the micropump remains significantly higher than the saturated vapor pressure of perfluorotriethylamine across the entire simulated temperature range (−37 °C to 72 °C). Consequently, the fluid remains entirely in the liquid phase.

2.1. Governing Equations

The governing equations are as follows:

(1) Mass conservation equation

$$\frac{\partial \rho_m}{\partial t} + \frac{\partial (\rho_m u_j)}{\partial x_j} = 0 \tag{1}$$

Here t denotes the time variable, ρ_m is the mixture density, and x_j and u_j correspond respectively to the spatial coordinates and the associated velocity components in the Cartesian frame.

(2) Momentum conservation equation

$$\frac{\partial (\rho_m u_i)}{\partial t} + \frac{\partial (\rho_m u_i u_j)}{\partial x_j} = -\frac{\partial p}{\partial x_i} + \frac{\partial}{\partial x_j}\left[(\mu_m + \mu_t)\left(\frac{\partial u_i}{\partial x_j} + \frac{\partial u_j}{\partial x_i} - \frac{2}{3}\frac{\partial u_k}{\partial x_k}\delta_{ij}\right)\right] + \rho_m g_i \tag{2}$$

where p is pressure, μ_m is the laminar viscosity coefficient of the fluid, μ_t is the turbulent viscosity coefficient. The term $\rho_m g_i$ in the momentum equation represents the gravitational body force.

(3) Energy equation

For the energy equation, one is the thermal energy equation (Thermal Energy, see Equation (3)), which is suitable for low-speed flow and cases where viscous effects can be neglected; the other is the total energy equation (Total Energy, see Equation (4)), which is suitable for high-speed flow and cases where viscous effects are considered, and also accounts for rotational energy.

$$\frac{\partial}{\partial t}[\rho_m h] + \frac{\partial}{\partial x_j}[\rho_m u_j h] = \nabla \cdot (k_{\text{eff}} \nabla T) \tag{3}$$

$$\frac{\partial}{\partial t}[\rho_m h_{\text{tot}}] - \frac{\partial p}{\partial t} + \frac{\partial}{\partial x_j}[\rho_m u_j h_{\text{tot}}] = \nabla \cdot (k_{\text{eff}} \cdot T) + \nabla \cdot (U \cdot \tau) \tag{4}$$

where $h_{\text{tot}} = h + \frac{1}{2}U^2$ is the total enthalpy, $h = C_{\text{pl}}T$ is the static enthalpy, k_{eff} is the effective thermal conductivity, $\nabla \cdot (U \cdot \tau)$ is the work done by viscous stresses.

2.2. Turbulence Model

Closure of the Reynolds-averaged Navier–Stokes equations is achieved via Menter's SST formulation, which transitions smoothly between the k-ϵ treatment (suitable for free-shear regions) and the k-ω treatment (appropriate for the near-wall layer) through a blending function. This characteristic makes it particularly well-suited for the present micropump flow, where strong wall-bounded shear layers, secondary flows, and localized separation coexist within the compact impeller–volute configuration [35,36]. The transport equation can be expressed as Equation (5).

$$\nu_t = \frac{\rho_m \alpha_1 k}{\max(\alpha_1 \omega, SF_2)} \tag{5}$$

and

$$\nu_t = \frac{\mu_t}{\rho_m} \tag{6}$$

The turbulent kinetic energy k equation is:

$$\frac{\partial(\rho_m k)}{\partial t} + \frac{\partial}{\partial x_j}(\rho_m U_j k) = P_k + \frac{\partial}{\partial x_j}\left[\left(\mu_m + \frac{\mu_t}{\sigma_{k3}}\right)\frac{\partial k}{\partial x_j}\right] - \beta' k\omega \tag{7}$$

The turbulent frequency ω equation is:

$$\frac{\partial(\rho_m \omega)}{\partial t} + \frac{\partial}{\partial x_j}\left[\rho_m U_j \omega - \left(\mu_m + \frac{\mu_t}{\sigma_{\omega 3}}\right)\frac{\partial \omega}{\partial x_j}\right] = \alpha_3 \frac{\omega}{k} P_k - \beta_3 \rho_m \omega^2 + 2(1 - F_1)\rho_m \frac{1}{\omega \sigma_{\omega 2}} \frac{\partial k}{\partial x_i}\frac{\partial \omega}{\partial x_i} \tag{8}$$

Here ν_t and μ_t denote respectively the kinematic eddy viscosity and the dynamic eddy viscosity; S is the invariant shear strain rate; α_1, σ_{k3}, β', $\sigma_{\omega 2}$, $\sigma_{\omega 3}$, α_3, β_1, and β_3 are calibrated model constants; and F_1 and F_2 are the blending functions that govern the transition between the two baseline formulations.

2.3. Entropy Production Theory

The second law of thermodynamics mandates that any irreversible process within a flowing fluid manifests as a positive entropy production rate. For the present micropump configuration, viscous dissipation constitutes the dominant irreversible mechanism; thermal dissipation is omitted from the analysis under the isothermal flow assumption. The entire fluid domain is initialized at a uniform temperature, and no external heat flux

is applied to the pump boundaries. Because the internal viscous heating is minimal, the temperature gradients (∇T) within the fluid are negligibly small. According to the entropy production framework, thermal entropy generation is proportional to the temperature gradients; thus, it is practically zero in this isothermal context. Furthermore, although the spacecraft thermal control loop experiences large temperature gradients globally across the radiators and heat sources, the fluid residence time within the micropump component itself is extremely short. Consequently, the medium temperature remains effectively uniform from the pump inlet to the outlet. Within the Reynolds-averaged framework, the total viscous entropy production is partitioned into two physically distinct contributions: (i) Entropy production rate by direct dissipation(EPDD), arising from the mean (time-averaged) velocity gradients, which captures large-scale shear losses, and (ii) Entropy production rate by turbulent dissipation(EPTD), originating from the fluctuating (turbulent) velocity gradients, which quantifies the dissipation associated with unresolved eddy motions. The mathematical expressions for these two components are given as follows:

$$\begin{aligned}\dot{S}_D''' = \frac{\mu_m}{T}\left[\left(\frac{\partial u_2'}{\partial x_1}+\frac{\partial u_1'}{\partial x_2}\right)^2+\left(\frac{\partial u_3'}{\partial x_1}+\frac{\partial u_1'}{\partial x_3}\right)^2+\left(\frac{\partial u_2'}{\partial x_3}+\frac{\partial u_3'}{\partial x_2}\right)^2\right] \\ +2\frac{\mu_m}{T}\left[\left(\frac{\partial u_1'}{\partial x_1}\right)^2+\left(\frac{\partial u_2'}{\partial x_2}\right)^2+\left(\frac{\partial u_3'}{\partial x_3}\right)^2\right]\end{aligned} \tag{9}$$

$$\begin{aligned}\dot{S}_{\overline{D}}''' = \frac{\mu_m}{T}\left[\left(\frac{\partial \overline{u_2}}{\partial x_1}+\frac{\partial \overline{u_1}}{\partial x_2}\right)^2+\left(\frac{\partial \overline{u_3}}{\partial x_1}+\frac{\partial \overline{u_1}}{\partial x_3}\right)^2+\left(\frac{\partial \overline{u_2}}{\partial x_3}+\frac{\partial \overline{u_3}}{\partial x_2}\right)^2\right] \\ +2\frac{\mu_m}{T}\left[\left(\frac{\partial \overline{u_1}}{\partial x_1}\right)^2+\left(\frac{\partial \overline{u_2}}{\partial x_2}\right)^2+\left(\frac{\partial \overline{u_3}}{\partial x_3}\right)^2\right]\end{aligned} \tag{10}$$

Wall-bounded entropy production, evaluated through the wall shear stress, is computed separately as:

$$\dot{S}_w^* = \frac{\tau_w u_p}{T} \tag{11}$$

where u_p is the near-wall velocity, τ_w denotes the wall shear stress.

The volumetric contributions are integrated over the respective fluid domains (impeller, volute, inlet, outlet) as follows:

$$\dot{S}_{\overline{D}} = \int_V \dot{S}_{\overline{D}}''' dV \quad \dot{S}_D = \int_V \dot{S}_D''' dV \quad \dot{S}_w = \int_A \dot{S}_w''' dA \tag{12}$$

$$\dot{S} = \dot{S}_{\overline{D}} + \dot{S}_D + \dot{S}_w \tag{13}$$

and the cumulative energy loss is obtained by time-integrating the entropy production rates:

$$I_{\overline{D}} = \int_V \dot{S}_{\overline{D}}''' dt dV \quad I_D = \int_V \dot{S}_D''' dt dV \tag{14}$$

$$I = I_{\overline{D}} + I_D + I_w \tag{15}$$

where $\dot{S}_{\overline{D}}'''$ and $\dot{S}_D'''$ are the entropy production rates contributed by the time-averaged and fluctuating velocity gradients, respectively, and $I_{\overline{D}}$ and I_D denote the associated cumulative energy losses.

2.4. Mesh Generation

The entire fluid volume—including the inlet section, impeller, and volute—was discretized exclusively with block-structured hexahedral cells (see Figure 1 for the mesh topology). Corresponding to "excellent" cell quality per the ANSYS Meshing criteria, and the average Skewness was below 0.1 across all sub-domains. To isolate discretization errors, five progressively refined meshes were generated by uniformly increasing the node count in all coordinate directions. For each grid resolution, a steady-state computation was performed at the design operating point, with the predicted head, shaft power, efficiency and total loss serving as the convergence metric. The head predictions exhibited a monotonic asymptotic trend, and the relative change between the third (3.65 million elements) and fourth resolution levels fell below 1%. Accordingly, the third mesh density was adopted for the full parametric campaign, striking an acceptable balance between numerical fidelity and computational throughput (Figure 2).

The numerical simulations were executed in ANSYS Fluent 2024, treating all solid boundaries as rigid walls. The COUPLED algorithm was employed for pressure–velocity coupling. Spatial discretization utilized the Second-Order Upwind scheme for momentum, turbulent kinetic energy, and specific dissipation rate to ensure higher-order accuracy. The temperature-dependent liquid-phase properties of perfluorotriethylamine over the interval $-37\ ^{\circ}\mathrm{C} \leqslant T \leqslant 72\ ^{\circ}\mathrm{C}$ were characterized through regression of experimental data, yielding the correlations summarized below: The temperature-dependent correlations for density, viscosity, specific heat capacity, and thermal conductivity of perfluorotriethylamine were obtained by polynomial fitting based on measured data over a temperature range of $-73\ ^{\circ}\mathrm{C}$ to $127\ ^{\circ}\mathrm{C}$. These measured data have been validated in our engineering projects. The measured data cover all the temperature conditions calculated in this paper.

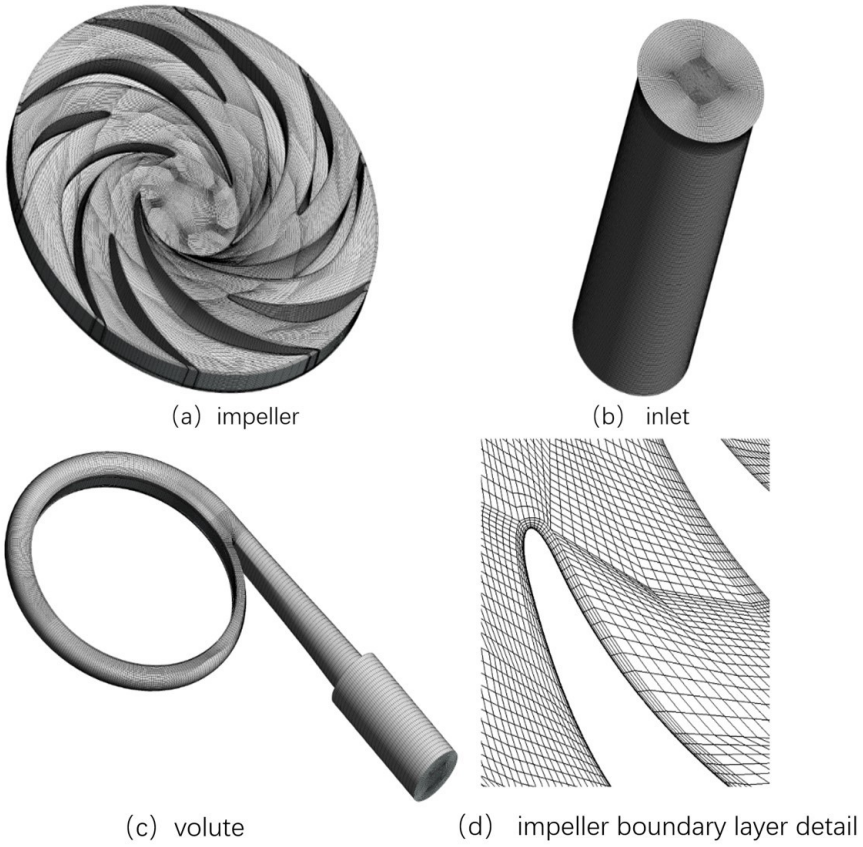


Figure 1. Mesh diagram of the space micropump fluid domain.

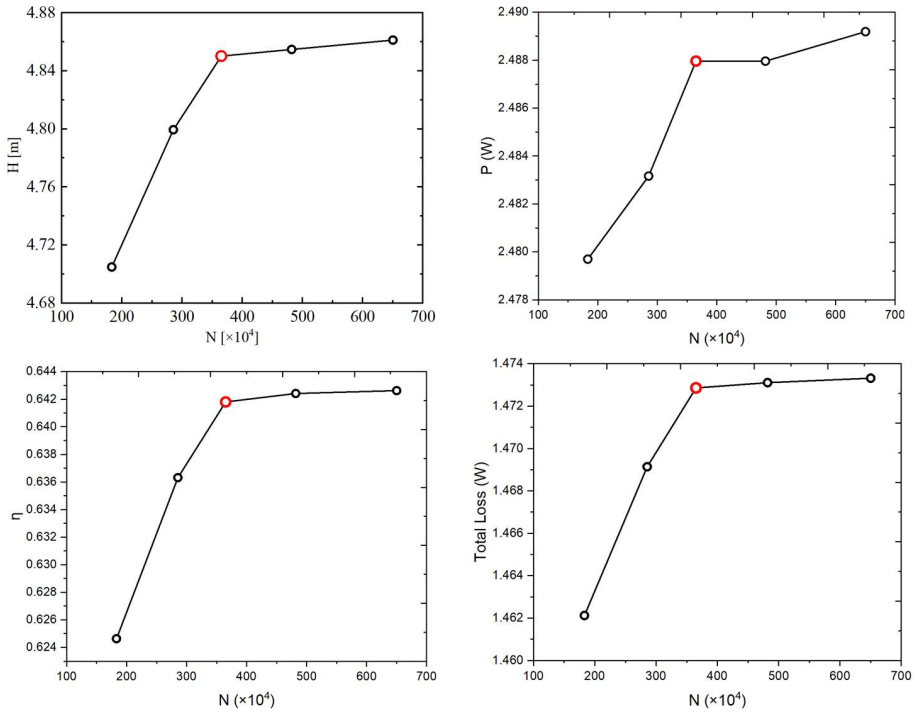


Figure 2. Head, shaft power, efficiency and total loss value at different mesh node counts.

(1) Density
Perfluorotriethylamine liquid density:

$$\rho_l = 2571.48157 - 2.80855T \tag{16}$$

(2) Viscosity
Perfluorotriethylamine liquid viscosity:

$$\mu_l = \frac{0.04954}{1 + \left(\frac{T}{203.9837}\right)^{13.8884}} + 0.00105 \tag{17}$$

(3) Specific heat capacity
Perfluorotriethylamine liquid specific heat capacity:

$$\begin{aligned} C_{pl} &= 1982.814356 + 0.609737T \\ &- 0.038704T^2 + 9.168609 \times 10^{-5}T^3 \end{aligned} \tag{18}$$

(4) Thermal conductivity
Perfluorotriethylamine liquid thermal conductivity:

$$\begin{aligned} \lambda_l &= 0.715804 - 0.005511T \\ &+ 1.015839 \times 10^{-5}T^2 + 5.439005 \times 10^{-9}T^3 \end{aligned} \tag{19}$$

(5) Standard state enthalpy:
For perfluorotriethylamine liquid, -3.1719×10^9 J/kmol;

2.5. Model Validation

To validate the accuracy of the numerical model calculations in this paper, performance tests were carried out on a micropump having the same geometry as the model. The tests were conducted at 25 °C with perfluorotriethylamine as the working fluid, an inlet pressure

of 0.2 MPa, and a rotational speed of 8000 rpm. The measured head values at different flow rates are compared with the computed results in the Figure 3 below. Near the design point, the deviation between the calculated and measured head is within 1.6%, whereas at off-design points, the maximum deviation reaches approximately 7%, demonstrating that the computational model adopted herein is highly reliable for subsequent research work at the rated operating point. Accordingly, the present paper will focus on quantitative analysis of the computational results near the rated point, while qualitative trend analyses will be performed for the off-design predictions.

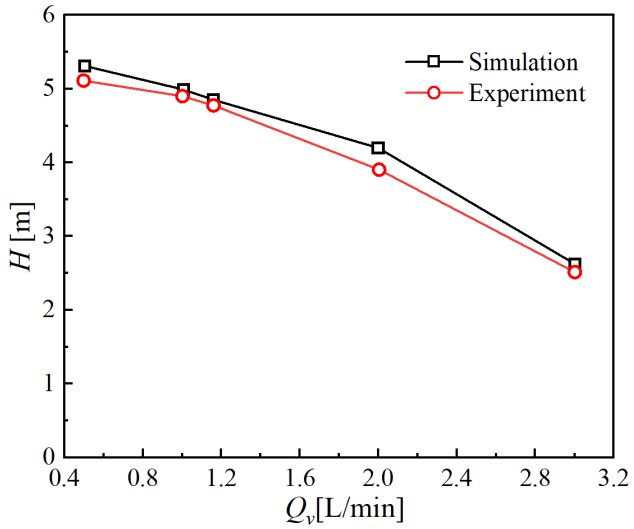


Figure 3. Comparison of calculated and measured pump flow-head characteristic.

To further justify the steady-state approach, an additional transient simulation was performed at the rated flow condition, and the time-averaged results were compared with the steady-state predictions, as summarized in Table 1. The time-averaged head, shaft power, efficiency, and integrated total entropy generation from the transient simulation deviated by less than 3% from the steady-state results. Because this study required a massive parametric sweep across multiple temperatures and flow rates, the steady-state approach was chosen for its computational efficiency without sacrificing macroscopic accuracy.

Table 1. Steady-state vs. transient results under rated conditions.

	H (m)	P (W)	η	Total Loss (W)
Steady	4.85022	2.48796	0.64184	1.47286
Transient	4.83686	2.49931	0.63712	1.48392

3. Study on the Influence of Different Inlet Temperatures on the Flow Characteristics of the Space Micropump

To investigate the external characteristics (head, shaft power, and efficiency), internal flow characteristics, and flow loss characteristics of the space micropump at different inlet temperatures, as well as the influence laws of temperature and flow rate on the internal flow characteristics and flow loss characteristics, numerical simulations were conducted at flow rates of 0.01 L/min, 0.5 L/min, 1 L/min, 1.16 L/min, 1.35 L/min, 1.5 L/min, 1.6 L/min, 1.7 L/min, 1.8 L/min, 2 L/min and 3 L/min.

3.1. Analysis of External Flow Characteristics at Different Inlet Temperatures

According to the flow rate-head characteristic curves of the space micropump at different inlet temperatures (Figure 4), the head curves at different temperatures have

consistent trends with small differences. As the temperature increases, the decrease in fluid viscosity plays a dominant role, resulting in a rise in head,as shown in Figure 5. At the rated flow rate, compared with the high temperature condition of 72 °C, the head under the low temperature condition of −37 °C decreases by approximately 5.37%.

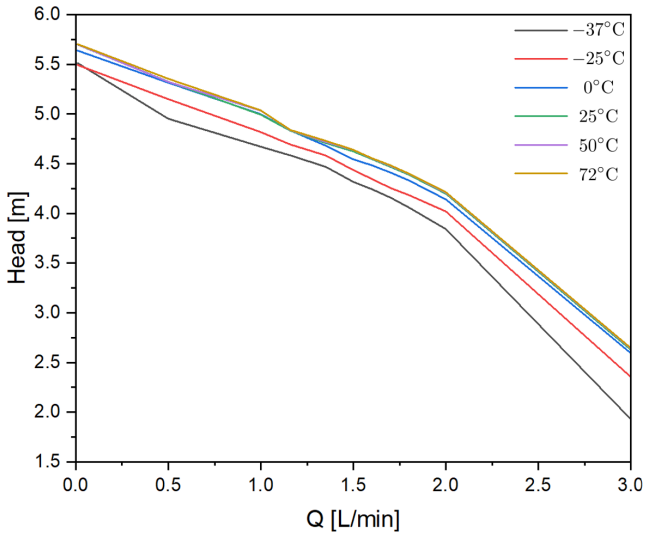


Figure 4. Head-flow rate characteristics at −37 °C to 72 °C.

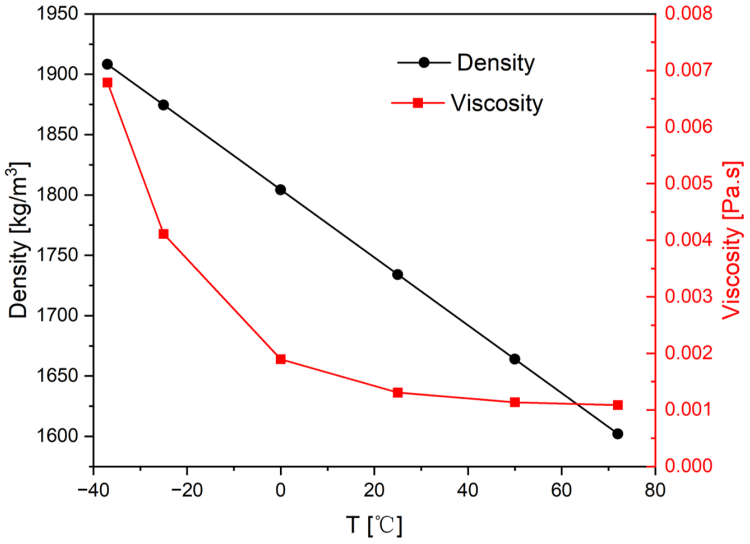


Figure 5. Density and dynamic viscosity of perfluorotriethylamine at various temperatures and atmospheric pressure.

As shown in Figure 6, for all temperature curves, the shaft power increases with increasing flow rate. This is because at higher flow rates, the pump requires more energy to overcome the fluid resistance and increase the fluid kinetic energy. The increase in shaft power is proportional to the increase in flow rate. At the same flow rate, the shaft power curves at different temperatures are relatively close but show subtle differences. Under rated operating conditions, the shaft power at the low temperature condition of −37 °C increases by 25.76% compared with that at the high temperature condition of 72 °C. This indicates that at lower temperatures, the fluid viscosity increases, leading to higher flow resistance, and consequently the micropump requires more energy to maintain the same flow rate.

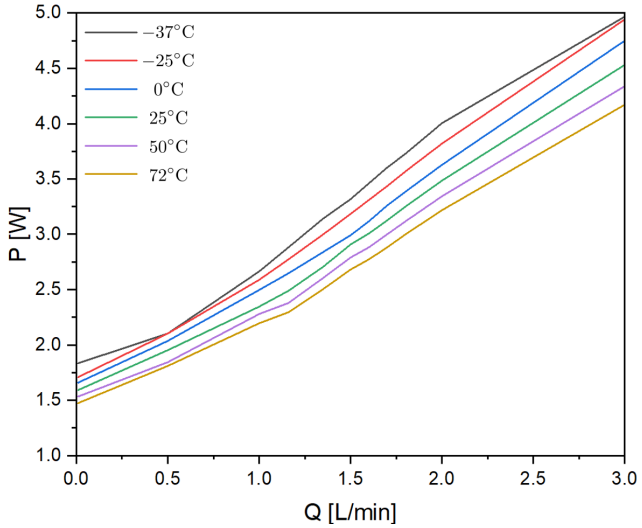


Figure 6. Shaft power-flow rate characteristics at −37 °C to 72 °C.

Figure 7 exhibits the efficiency-flow rate external characteristic curves at different temperatures. For all tested temperatures, the space micropump maintains high efficiency within the flow rate range of 1 L/min to 2 L/min, beyond which efficiency declines with increasing flow rate. At −37 °C and −25 °C, the peak efficiency occurs at a relatively lower flow rate of approximately 1.5 L/min. As the temperature rises, the flow rate corresponding to the peak efficiency increases slightly. Below 0 °C, the efficiency curves shift upward rapidly with increasing temperature. Above 0 °C, the efficiency curves at different temperatures nearly coincide, indicating that efficiency is less sensitive to temperature in this range. According to Figure 5, the viscosity of the working fluid exhibits only minor variations above 0 °C, suggesting that the efficiency of the space micropump is strongly influenced by the viscosity of the working fluid. Overall, under rated operating conditions, the efficiency at the low temperature condition of −37 °C decreases by 10.15% compared with that at the high temperature condition of 72 °C.

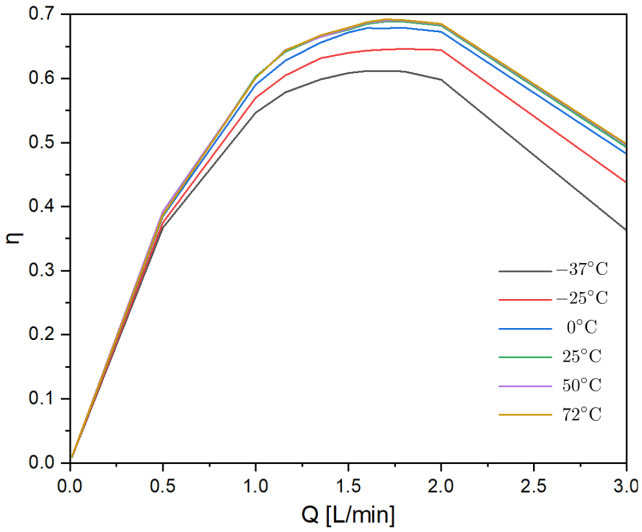


Figure 7. Efficiency-flow rate characteristics at −37 °C to 72 °C.

Figure 8 illustrates the variation in head of the space micropump at different inlet temperatures under the rated flow rate. The head increases with increasing temperature until 0 °C, after which the head stabilizes with further temperature increase. At low temperatures, the fluid viscosity decreases as the temperature rises, reducing internal friction in

the pump and thereby increasing the head. At higher temperatures, the fluid viscosity does not change significantly with temperature, and the head varies little with temperature.

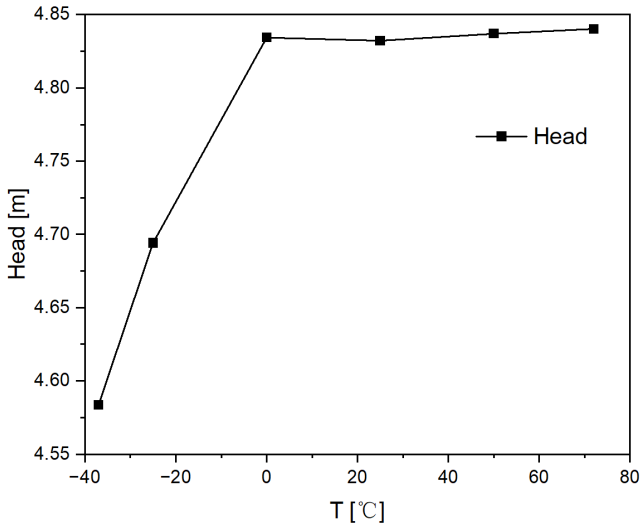


Figure 8. Variation curve of head with inlet temperature at 8000 rpm, 1.16 L/min.

Figure 9 presents the variation in shaft power of the space micropump at different inlet temperatures under the rated flow rate. The shaft power decreases with increasing temperature. The decreasing trend of shaft power indicates that the pump operates more efficiently at higher temperatures, requiring less power input.

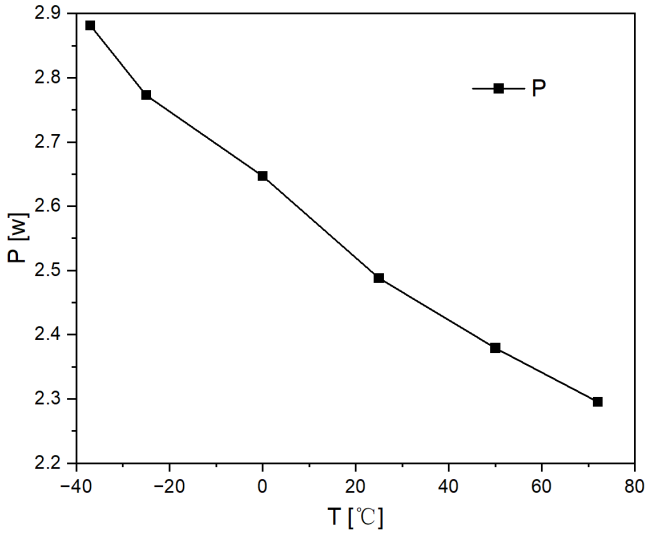


Figure 9. Variation curve of shaft power with inlet temperature at 8000 rpm, 1.16 L/min.

Figure 10 shows the variation in efficiency of the space micropump at different inlet temperatures under the rated flow rate. The efficiency increases with increasing temperature until it reaches a peak and then begins to level off. Between −37 °C and 0 °C, the efficiency increases rapidly, indicating that temperature has a significant positive effect on efficiency in this temperature range. From 0 °C to approximately 25 °C, the efficiency continues to increase but at a slower rate, and then between 25 °C and 72 °C, the efficiency changes little and tends to stabilize. Consistent with the variation in head with temperature, this is because the fluid viscosity decreases significantly as the temperature rises at low temperatures, reducing internal friction in the pump and thereby improving both efficiency and head. At higher temperatures, the fluid viscosity does not change significantly with temperature, and both head and efficiency vary little with temperature.

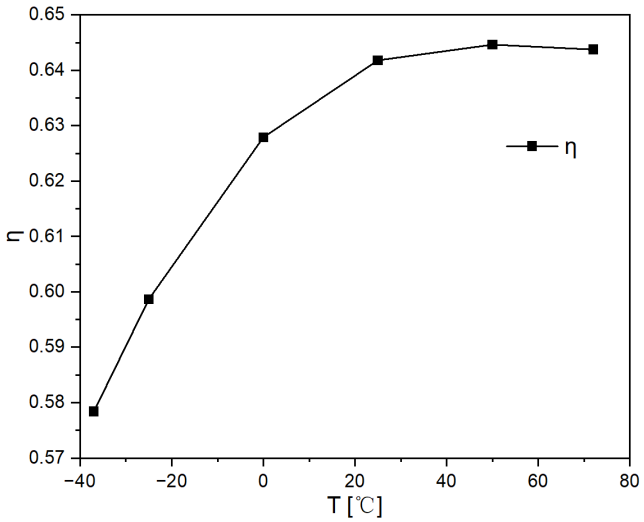


Figure 10. Variation curve of efficiency with inlet temperature at 8000 rpm, 1.16 L/min.

3.2. Analysis of Internal Flow Characteristics at Different Inlet Temperatures

3.2.1. Analysis of the Influence on Pressure Distribution

As shown in Figure 11, it can be seen from the contour that the pressure distribution exhibits obvious rotational symmetry. At high temperature (72 °C), the pressure distribution is relatively uniform, and the transition between high-pressure and low-pressure regions is relatively smooth. The position with the highest pressure is near the volute tongue, where the pressure rises after the fluid impacts the tongue. As the temperature decreases, the high-pressure region gradually expands. At low temperatures, the increased fluid viscosity requires the pump to exert greater force to drive the fluid.

Temperature governs the internal flow regime primarily by altering fluid viscosity. Low-temperature operation increases viscosity and flow resistance, culminating in a distinct high-pressure agglomeration in the impeller region. In contrast, elevated temperatures reduce viscosity, thus flattening the pressure gradient and yielding a more uniform pressure distribution with diminished high-pressure extents.

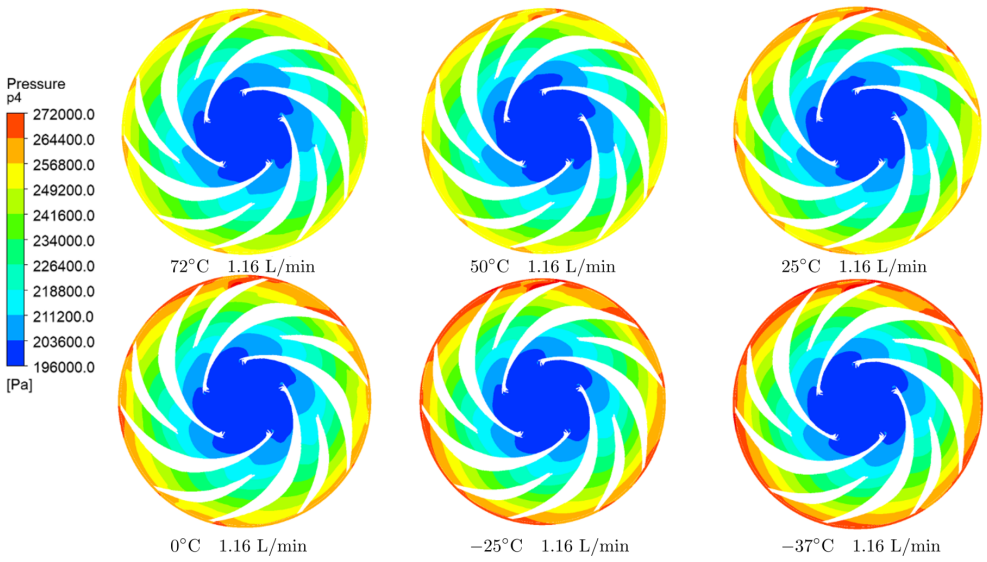


Figure 11. Pressure distribution contour of the impeller axial section at 8000 rpm, 1.16 L/min and different inlet temperatures.

Figure 12 illustrates the pressure field evolution within the space micropump at a flow rate of 1.16 L/min across the prescribed temperature range. At all tested temperatures, the volute exhibits a qualitatively similar global pressure topology, characterized by a circumferentially mild pressure variation along the impeller shroud and a generally uniform baseline distribution. However, a systematic elevation in local pressure at identical peripheral locations is observed as temperature decreases. This thermo-induced pressurization is attributable to the viscosity-driven augmentation of hydraulic impedance: the elevated viscosity at low temperatures intensifies frictional losses, which promotes the conversion of dynamic pressure into static pressure rise along the flow path. Conversely, elevated temperatures reduce viscous dissipation, thereby flattening the peripheral pressure gradient and yielding a more homogeneous field. Notably, the most pronounced temperature sensitivity emerges in the volute tongue vicinity, where low-temperature operation steepens the local pressure gradient due to the combined effects of reduced Reynolds number and intensified boundary-layer shear.

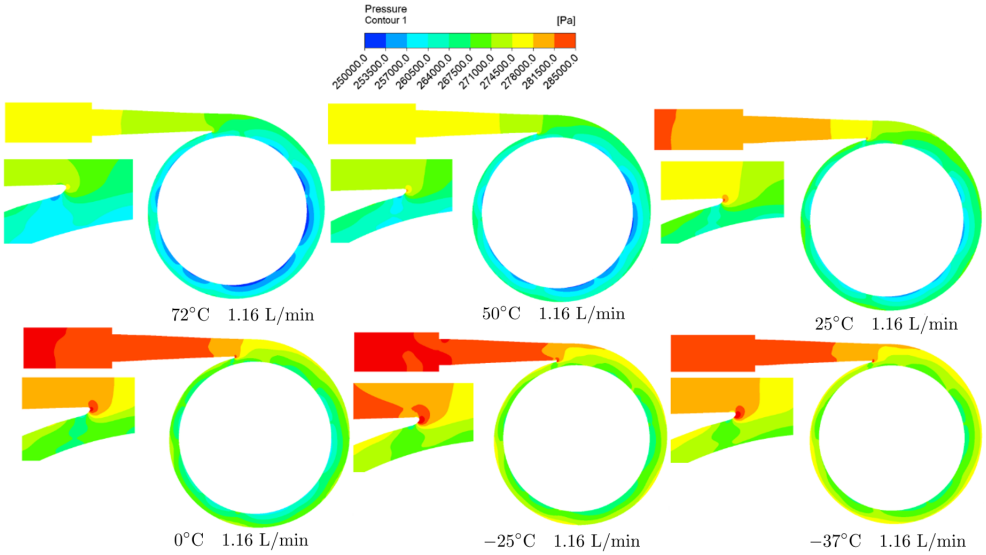


Figure 12. Pressure distribution contour of the volute axial section and local enlargement of the volute tongue at 8000 rpm, 1.16 L/min and different inlet temperatures.

Figure 13 displays the space micropump at different flow rates of −37 °C and 72 °C under the axial section pressure distribution contour of the impeller region. Increased flow rate leads to decreased head and static pressure in the volute, and the static pressure gradient variation in the entire flow field decreases. At higher flow rates, the pressure distribution in the impeller region is more uniform, while at lower flow rates, the pressure distribution shows more obvious high-pressure regions at the impeller outlet. At −37 °C and 72 °C, the variation trend of the impeller mid-axial section pressure distribution with flow rate is essentially the same.

Figure 14 illustrates the space micropump at different flow rates of −37 °C and 72 °C at volute region axial section pressure distribution contour. As flow rate increases, the pressure variation within the flow passage at the impeller tip remains small. An exception is observed only at −37 °C and 0.5 L/min, where the pressure is notably higher than under other flow conditions. At 72 °C and 2 L/min, a low-pressure region appears near the tongue. This is attributed to the low viscosity and high flow velocity at this temperature, which cause substantial flow losses upon fluid impingement against the tongue, resulting in a marked pressure drop. As the flow rate decreases, the pressure at the tongue becomes significantly higher than that near the impeller tip. Meanwhile, the pressure at the outlet rises, and the high-pressure zone extends toward the tongue.

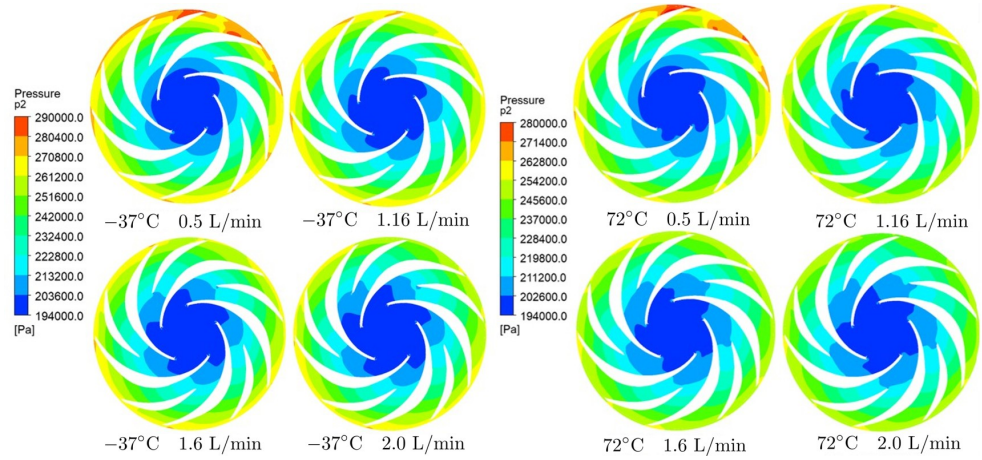


Figure 13. At different flow rates, −37 °C and 72 °C impeller mid-axial section pressure distribution contour.

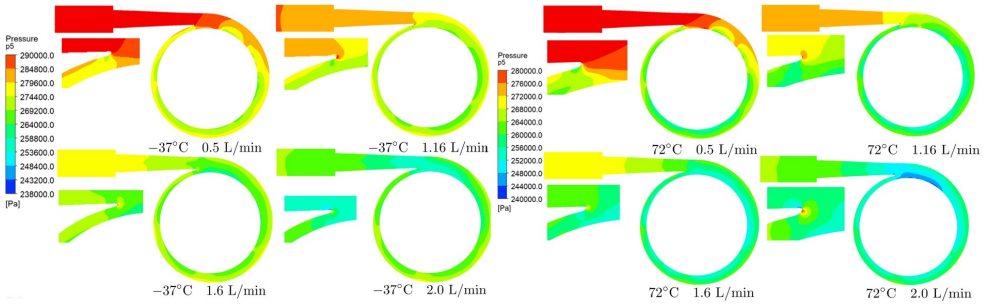


Figure 14. At different flow rates, −37 °C and 72 °C volute mid-axial section pressure distribution contour and local enlargement of the volute tongue.

3.2.2. Analysis of the Influence on Streamline Distribution

Figure 15 shows the space micropump at different flow rates of −37 °C and 72 °C in the impeller mid-axial section streamline diagram. At all temperatures, the streamlines in the flow channel between the working surface of the long blade and the short blade are straight and smooth, with high velocity and small flow losses. In contrast, the streamlines in the flow channel between the back surface of the long blade and the working surface of the short blade are relatively disordered, forming one or more vortices of varying sizes, with low velocity, nearly stagnant flow, and large flow losses. The vortex morphology is more pronounced in the flow channels near the volute tongue, while the vortex morphology is less obvious in the flow channels farther from the tongue. The short blades separate the stable flow region from the unstable flow region. At the impeller outer edge position near the tongue, the velocity gradient in the flow channel is extremely large, and the velocity at this position in the impeller reaches its maximum, because the volute flow channel cross-sectional area at this location is small, resulting in accelerated flow.

Under high-temperature conditions, there are more vortices in the flow channels near the volute tongue. As the temperature decreases, the vortex morphology at the impeller outer edge gradually becomes less defined. At −37 °C, the vortices at the impeller outer edge disappear completely, indicating that as the temperature decreases, the fluid viscosity increases, the turbulent dissipation effect weakens, flow separation is suppressed, and the flow stability inside the impeller improves.

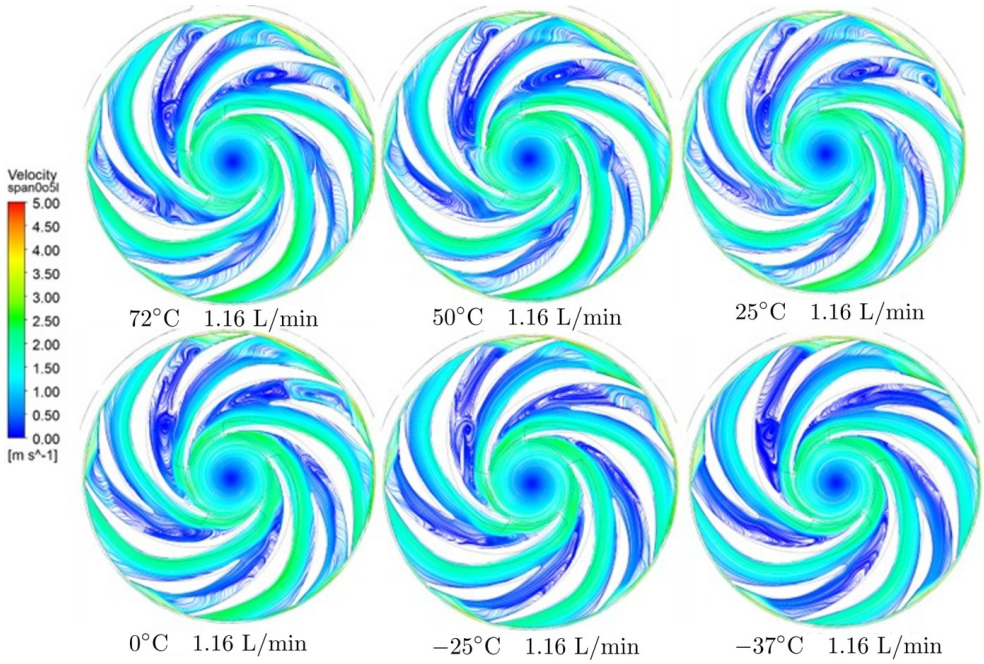


Figure 15. Streamline diagram of the mid-axial section at different temperatures.

Figure 16 displays the space micropump at different flow rates of −37 °C and 72 °C in the volute mid-axial section streamline diagram. At all temperatures, the fluid in the volute flow channel at the impeller outer edge flows relatively smoothly. After being subjected to the centrifugal action of the impeller, the fluid approaches the volute wall and flows along the volute toward the outlet. After passing the tongue position, the flow channel cross-sectional area gradually increases, the flow velocity decreases and the pressure increases. At the pump outlet, due to the presence of a diffuser, asymmetric vortices are generated in the upper and lower regions after the fluid enters the diffuser.

At 72 °C, two relatively large vortices appear below the outlet. As the temperature decreases, the two large vortices begin to merge into a single large vortex. Below 0 °C, the two vortices completely merge together. The vortex appearing above the outlet is almost unaffected by temperature changes.

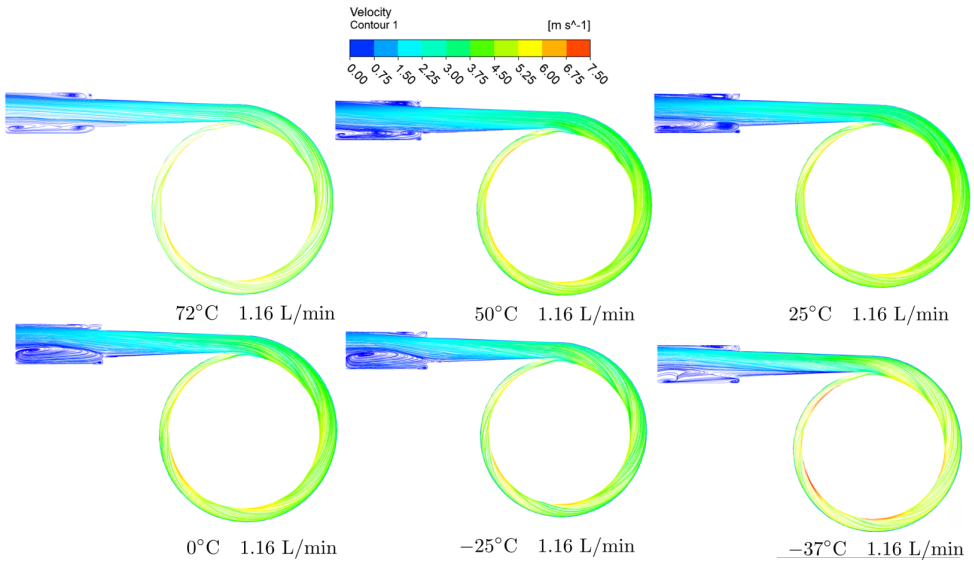


Figure 16. Streamline diagram of the volute mid-axial section at 8000 rpm, 1.16 L/min and different temperatures.

Figure 17 presents the space micropump at different flow rates of −37 °C and 72 °C in the impeller mid-axial section streamline diagram. At all temperatures, the fluid velocity in the volute connected to the flow channel between the working surface of the long blade and the back surface of the short blade is relatively high, and after friction with the surrounding low-velocity fluid, the velocity decreases, reaching its lowest near the volute wall.

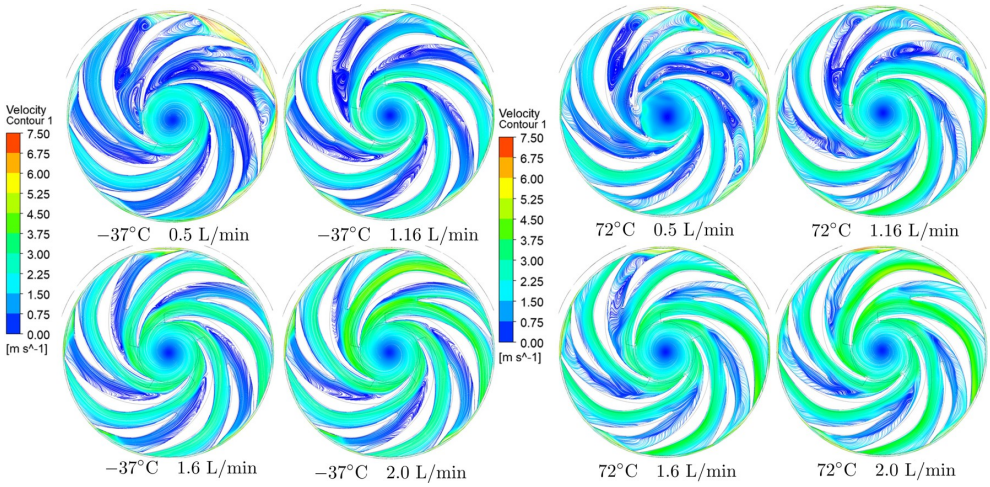


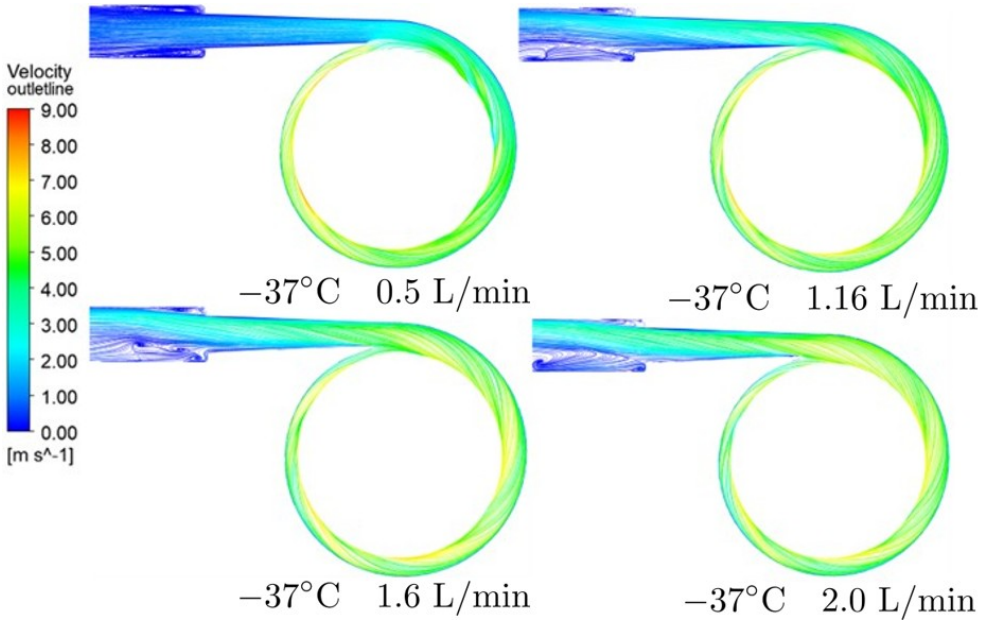
Figure 17. At different flow rates, −37 °C and 72 °C impeller mid-axial section streamline diagram.

Figure 18 shows the space micropump at −37 °C and 72 °C and at different flow rates in the volute region mid-axial section streamline diagram. At 72 °C, 0.5 L/min, the flow velocity in the left side of the volute is significantly higher than in the right side. At the outlet, the streamlines are compressed by the vortices on the upper side, causing the fluid entering the outlet to shift downward. As the flow rate increases, the velocity gradient along the volute direction decreases, the flow velocity gradually becomes uniform, and the fluid entering the outlet gradually shifts upward. At 72 °C, 2 L/min, owing to the high flow rate and correspondingly high velocity, the flow begins to squeeze the vortices above and below. A slightly different behavior is observed at −37 °C. At 0.5 L/min, the fluid enters the outlet and distributes centrally, with relatively symmetric vortices on both sides. Under other flow conditions, the vortex morphology at the outlet becomes unclear. This is attributed to the high viscosity of the fluid at low temperatures, which weakens turbulent dissipation and thereby suppresses vortex formation.

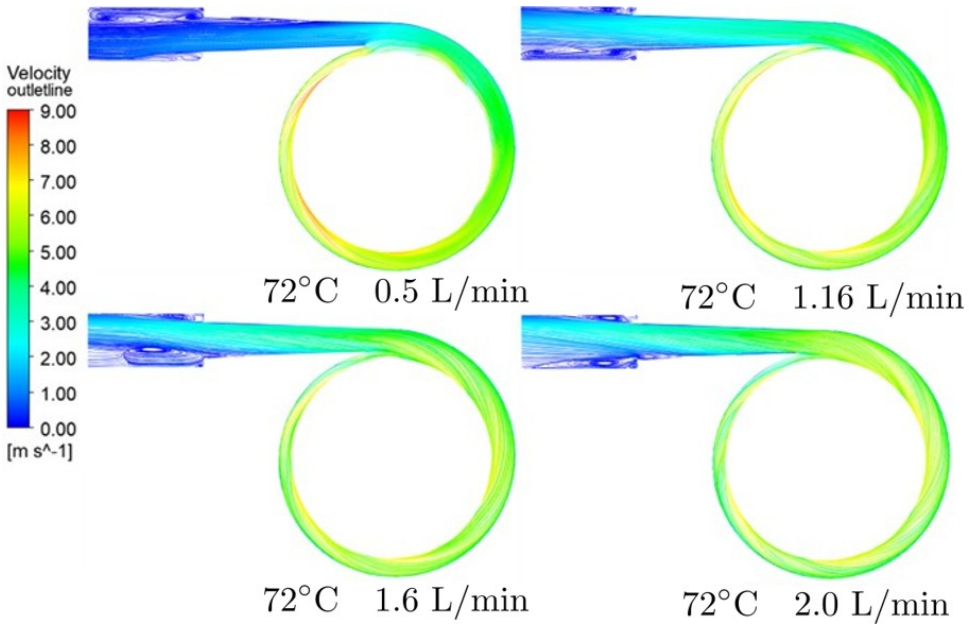
3.2.3. Analysis of the Influence on Turbulent Kinetic Energy Distribution

Figure 19 demonstrates the space micropump at rated flow rate at different temperatures in the impeller mid-axial section turbulent kinetic energy distribution contour diagram. In all figures, the high turbulent kinetic energy region is mainly distributed at the impeller outer edge position. The turbulent kinetic energy is even higher in the impeller outer edge region between the back surface of the long blade and the working surface of the short blade, and the turbulent kinetic energy is highest near the volute tongue, which is also the location with the maximum velocity gradient. There is also a relatively high turbulent kinetic energy strip-shaped region at the back surface of the long blade leading edge, which develops and disappears near the middle of the long blade. The turbulent kinetic energy in the hub region is relatively low, indicating that the turbulence intensity of the fluid near the hub is small. This is because the hub is the inlet where the fluid enters the impeller, and the fluid is accelerated by the impeller at this location, but the turbulence has not yet fully developed. As the temperature decreases, the maximum turbulent kinetic energy decreases, the turbulent kinetic energy at the impeller outer edge position changes little, and the turbulent kinetic energy strip generated at the back surface of the long blade

gradually shrinks and even disappears. The distribution of turbulent kinetic energy is related to the viscosity of the fluid. At high temperatures, the low viscosity does not help reduce turbulent dissipation, thereby increasing the turbulent kinetic energy.



(**a**) −37 °C



(**b**) 72 °C

Figure 18. At different flow rates, −37 °C and 72 °C volute mid-axial section streamline diagram.

Figure 20 presents the turbulent kinetic energy (TKE) distribution contours on the mid-axial section of the volute at rated flow rate across the temperature spectrum. At all thermal conditions, the TKE exhibits a monotonic decay from the impeller outlet toward the volute discharge, indicating progressive flow deceleration and corresponding attenuation of turbulence intensity along the collecting channel. Elevated TKE levels are observed in the curved volute passages, attributable to the centrifugal instability induced by streamline curvature. The tongue region consistently harbors the highest TKE, where the local flow turning and acceleration generate intense shear. In contrast, the pump outlet

region displays markedly lower TKE, confirming that the turbulence has been substantially damped through the decelerating diffusive flow within the volute. Regarding thermal effects, decreasing temperature induces marginal variations in TKE at the impeller periphery, yet notably suppresses the peak TKE in the tongue-adjacent high-intensity zone, while slightly elevating the outlet TKE level.

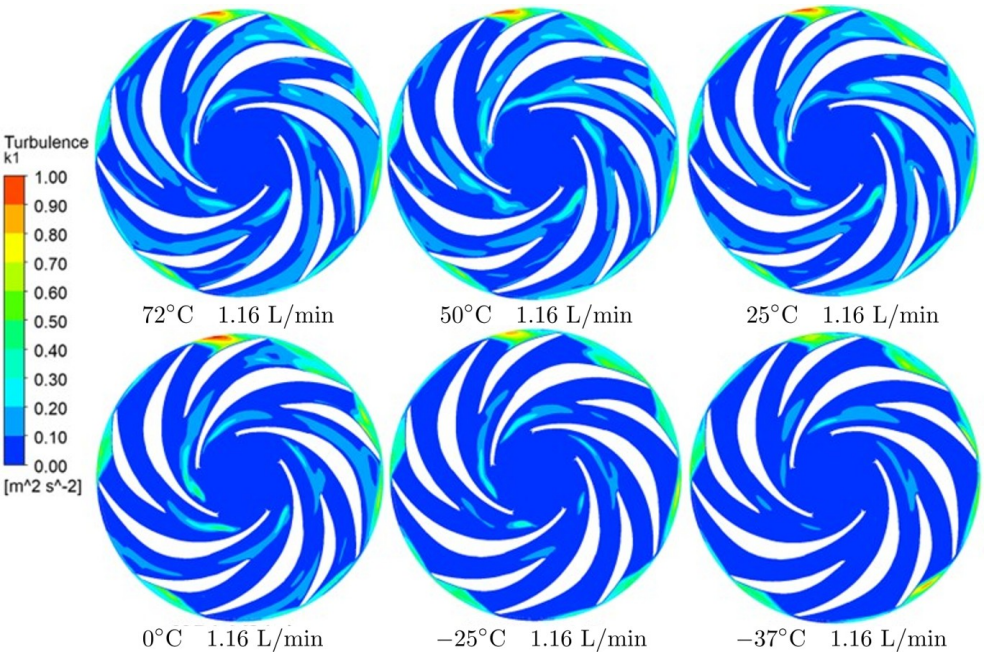


Figure 19. Turbulent kinetic energy distribution diagram of the impeller mid-axial section at 8000 rpm, 1.16 L/min and different temperatures.

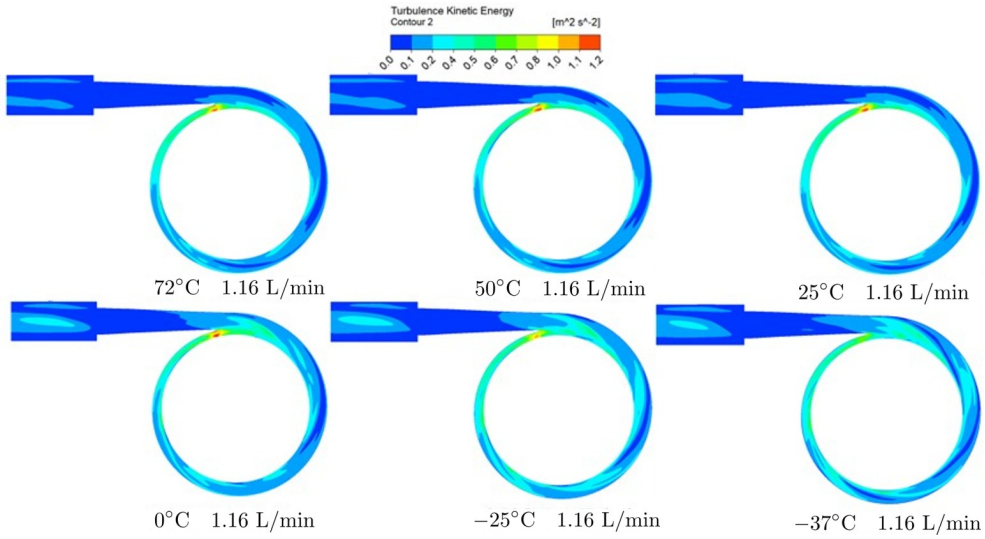


Figure 20. Turbulent kinetic energy distribution diagram of the volute mid-axial section at 8000 rpm, 1.16 L/min and different temperatures.

Figure 21 displays the space micropump at −37 °C and 72 °C and different flow rates in the impeller region mid-axial section turbulent kinetic energy distribution contour. At −37 °C, 0.5 L/min, the high turbulent kinetic energy region is mainly distributed at the impeller outer edge position. The turbulent kinetic energy in the impeller outer edge region between the back surface of the long blade and the working surface of the short blade is higher than that in the impeller outer edge region between the working surface of the long blade and the back surface of the short blade. In addition to the extremely high turbulent

kinetic energy near the tongue, a high turbulent kinetic energy region also appears at the next blade period position. As the flow rate increases, the high turbulent kinetic energy region shrinks, and the extreme turbulent kinetic energy region rapidly disappears. At 72 °C, the variation trend of turbulent kinetic energy with flow rate is essentially the same.

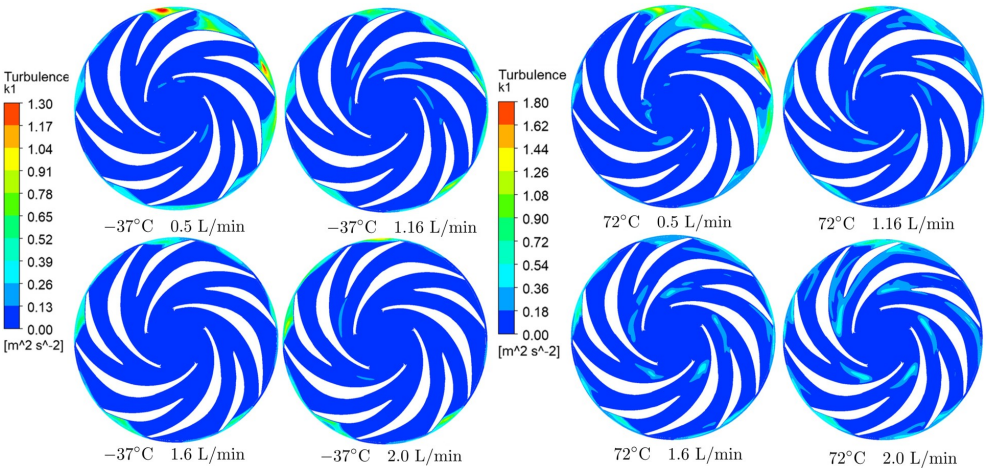


Figure 21. Different flow rates −37 °C and 72 °C impeller mid-axial section turbulent kinetic energy distribution diagram.

Figure 22 presents the turbulent kinetic energy (TKE) distribution contours on the mid-axial section of the volute at −37 °C and 72 °C across a range of flow rates. At −37 °C and 0.5 L/min, the high-TKE regions are predominantly localized near the impeller–tongue clearance and several discrete peripheral locations. As flow rate increases, the TKE magnitude within the impeller-peripheral high-intensity zone progressively diminishes, while the spanwise TKE distribution becomes increasingly uniform. Concurrently, the TKE level at the pump outlet rises monotonically, indicating enhanced turbulent dissipation prior to discharge. This trend is physically consistent with the alleviation of flow blockage and separation within the impeller passages at higher flow rates—where the improved through-flow condition suppresses local shear while the elevated exit velocity concurrently intensifies outlet turbulent mixing. At 72 °C, the same qualitative trends are observed, albeit with systematically lower TKE magnitudes across most regions, attributable to the reduced fluid viscosity and weakened shear layer intensity at elevated temperatures.

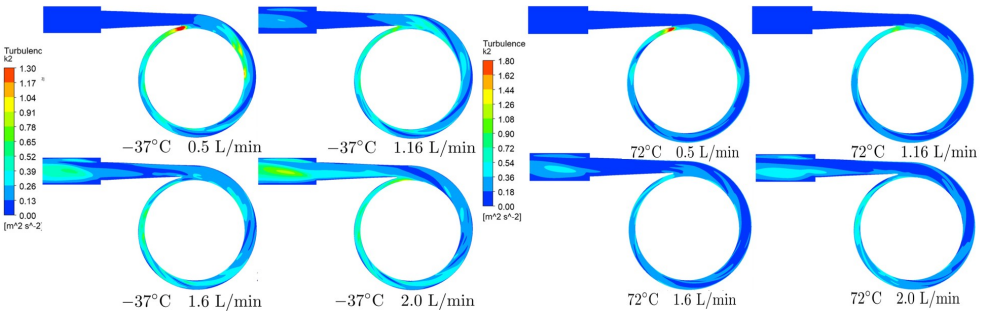


Figure 22. Different flow rates −37 °C and 72 °C volute mid-axial section turbulent kinetic energy distribution diagram.

3.3. Flow Loss Analysis of the Space Micropump at Different Inlet Temperatures

As shown in Figure 23, the loss values at each position vary at different temperatures. Across all thermal conditions, the volute consistently emerges as the dominant loss contributor, with its share of the total entropy production far exceeding that of the inlet and shroud regions, accounting for over 34%. By contrast, the inlet section contributes negligibly to

the overall dissipation budget. Overall, the volute, upper shroud, and impeller regions account for relatively large loss proportions in the entire system, and these regions are the main sources of entropy production. As temperature increases, the loss proportion of the impeller region rises, while losses at other positions (except for the volute) decrease. With rising temperature, fluid viscosity decreases, leading to reduced flow resistance and energy losses, and losses at all positions decline. Compared with the low temperature condition of −37 °C, the total loss at the high temperature condition of 72 °C decreases by approximately 46.9%.

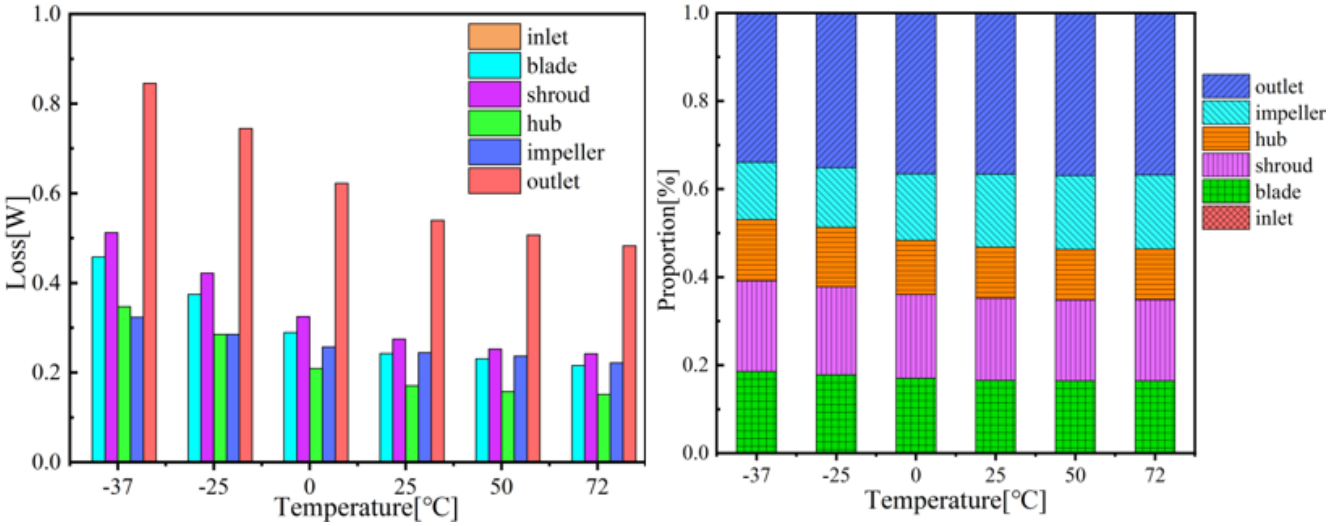


Figure 23. Loss magnitude and proportion at different positions of the pump at 8000 rpm, 1.16 L/min and different inlet temperatures.

Figure 24 illustrates the space micropump at −37 °C and 72 °C and at different flow rates, all region loss and proportion bar chart. At 72 °C and different flow rates, the outlet losses are higher, the inlet position losses are extremely small, and the losses at other positions are similar in magnitude. As the flow rate increases, the losses at all positions first decrease and then increase, all reaching their minimum values at the rated flow rate, with energy losses increasing significantly at large flow rates. At −37 °C, the losses at all positions nearly doubled, as the increased flow resistance at low temperatures leads to increased flow losses inside the pump.

The loss proportions of the outlet and impeller are relatively large in the entire system, indicating that these regions are the main sources of entropy production. The loss proportions of the lower shroud and upper shroud are relatively small, because the flow in these regions is relatively stable, with less entropy production.

Figure 25 shows the space micropump at rated flow rate at different temperatures in the impeller mid-axial section entropy production rate distribution contour. Under high-temperature conditions (72 °C and 50 °C), the entropy production losses are mainly concentrated near the leading and trailing edges of the blades, while the entropy production loss values at the connections between the impeller hub and the blades are relatively low. The area proportion of the high entropy production loss regions is small, and the distribution is relatively isolated. This indicates that at higher temperatures, the fluid flow is relatively smooth, and energy losses are mainly concentrated in regions where effects such as local flow separation and boundary layer friction are more pronounced. As the temperature decreases, the range of high entropy production loss regions expands somewhat, especially with increased entropy production loss values in the regions near the middle of the blades. As the temperature drops to 0 °C and below, the distribution characteristics of entropy production losses undergo significant changes. In the entire

impeller region, the area of high entropy production loss regions increases significantly, almost covering most of the blade surfaces and a large range of the impeller hub. Especially at −25 °C and −37 °C, the high entropy production regions continue to expand and merge into a continuous area. This indicates that as the temperature decreases, the fluid viscosity increases and the flow resistance increases, thereby intensifying the energy losses, and the entropy production losses become more uniformly distributed throughout the impeller region.

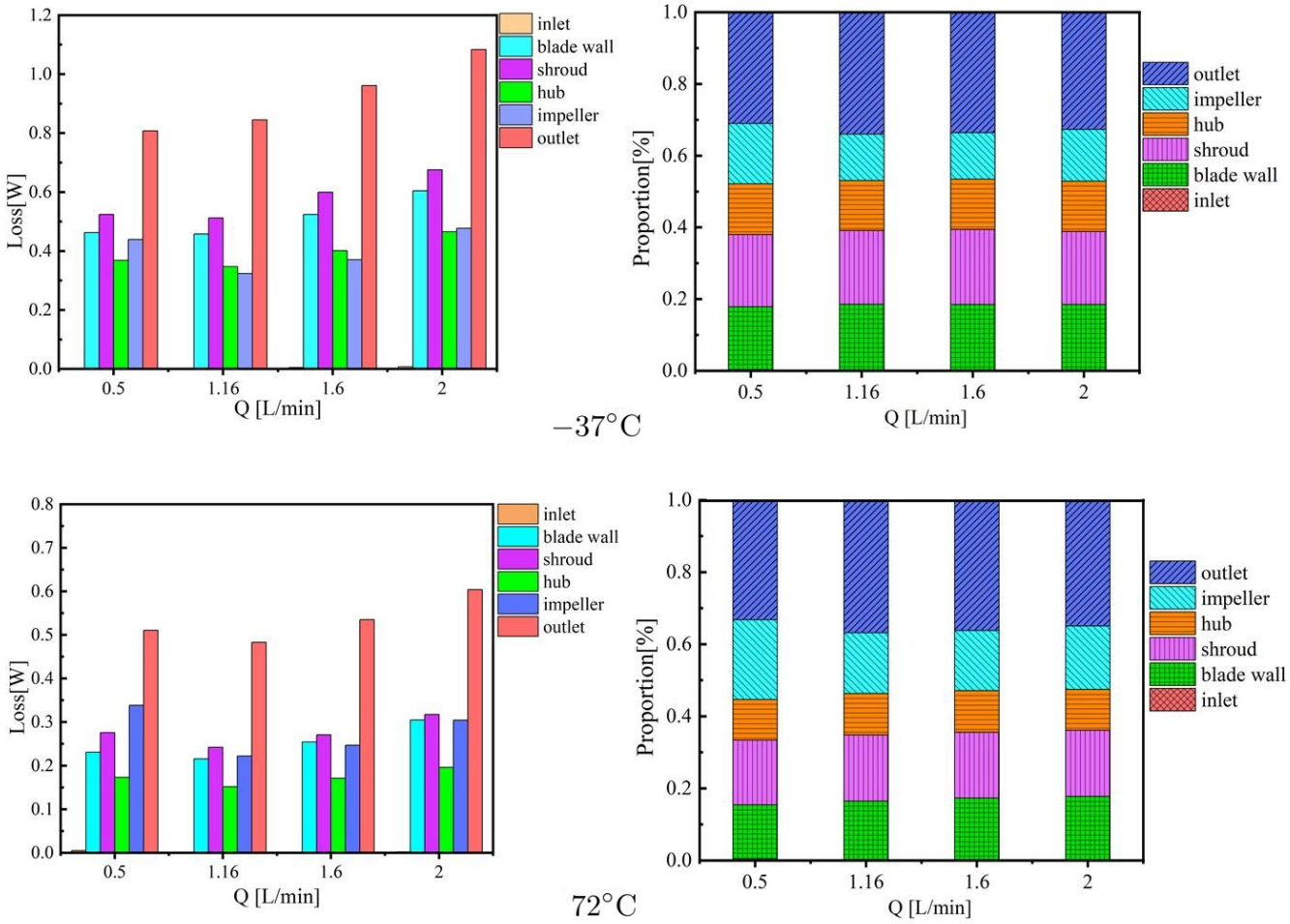


Figure 24. At different flow rates, −37 °C and 72 °C pump loss magnitude and proportion at different positions.

Under low-temperature conditions, the high entropy production loss region in the hub area and the high entropy production loss region on the blades become interconnected, forming a larger high entropy production loss region. This is because the fluid flow near the hub encounters greater resistance at low temperatures, leading to increased energy losses, and this influence is transmitted to the blades through the fluid flow.

Therefore, temperature has a significant influence on the entropy production loss distribution of the impeller. As the temperature decreases, the entropy production loss distribution range gradually expands, with more high entropy production loss regions and a more complex distribution.

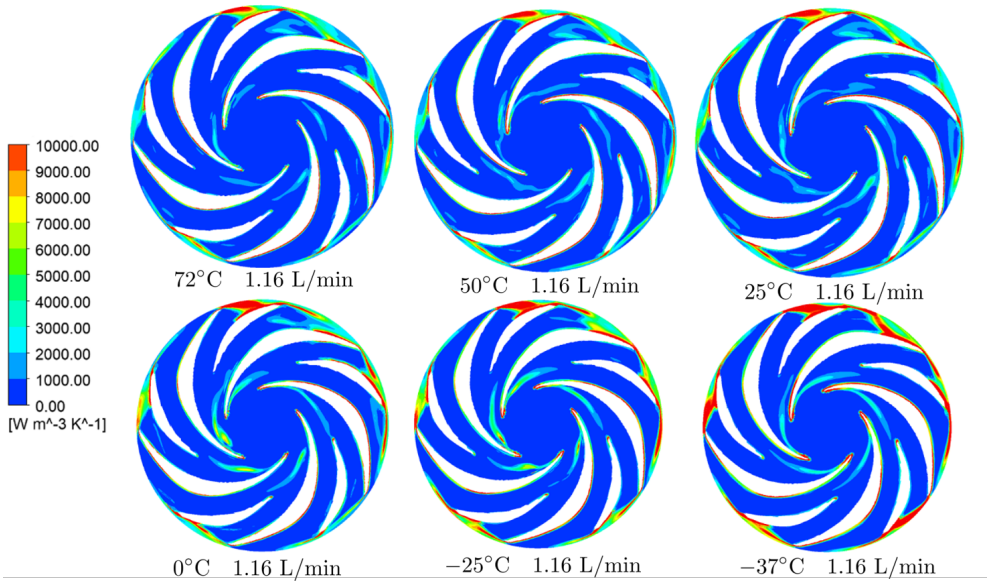


Figure 25. Entropy production rate distribution contour of the impeller mid-axial section at 8000 rpm, 1.16 L/min and different temperatures.

Figure 26 presents the space micropump at rated flow rate at different temperatures in the volute mid-axial section turbulent kinetic energy distribution contour. The high entropy production regions are mainly distributed in the volute flow channel at the impeller outer edge, near the volute tongue and near the volute outer wall. The entropy production rate at other positions in the volute is slightly lower, and the entropy production rate at the outlet is the lowest. Under high-temperature (72 °C) conditions, the entropy production rate is highest near the tongue and gradually decreases along the blade rotation direction. The entropy production rate near the volute outer wall is also relatively high, but the distribution region presents an extremely narrow strip shape. As the temperature decreases, the range of the high entropy production rate region near the tongue expands, and the area of the sub-high entropy production rate region along the blade rotation direction slightly expands. When it is 0 °C and below, high entropy production rate distribution regions also appear at other positions in the volute flow channel at the impeller outer edge besides near the tongue, and the strip of the high entropy production rate distribution region near the volute outer wall becomes wider.

Temperature has a very significant effect on the entropy production rate in the volute flow channel, near the tongue, and at the outlet. As the temperature decreases, the fluid viscosity increases, causing the fluid to encounter greater resistance during flow inside the pump, generating more turbulence and vortices, thereby increasing the entropy production rate. At high temperatures, the fluid viscosity is lower, the flow is more stable, and the entropy production rate is lower. At low temperatures, generating more local disturbances and vortices, leading to higher energy losses and entropy production.

Figure 27 presents the entropy production rate (EPR) contours on the lower shroud wall of the space micropump at rated flow rate under varying thermal conditions. On the working surfaces, the long blade—owing to its larger contact area—plays a dominant role in flow guidance and exhibits substantial friction-induced losses. At cryogenic temperatures (e.g., −37 °C), the elevated viscosity intensifies wall shear, resulting in markedly high EPR. As temperature rises to 72 °C, the viscosity reduction attenuates frictional dissipation, and the EPR decreases correspondingly. The short blade working surface, despite its shorter flow path, features a more compact geometry that amplifies local velocity gradients; consequently, its EPR at low temperatures remains comparably high, yet the thermal-induced reduction is less pronounced than that of the long blade, rendering the short

blade more intrinsically susceptible to turbulent fluctuations. On the suction surfaces, the long blade exhibits elevated EPR at low temperatures due to flow separation and vortex formation within low-pressure zones. With increasing temperature, the enhanced fluid kinetic energy suppresses the separation zone, leading to a marked EPR reduction. The short blade suction surface, characterized by more severe geometric discontinuities, is inherently more prone to strong vortex generation; its EPR exceeds that of the long blade at cryogenic conditions, and the EPR diminishes more rapidly at elevated temperatures as the turbulence intensity subsides.

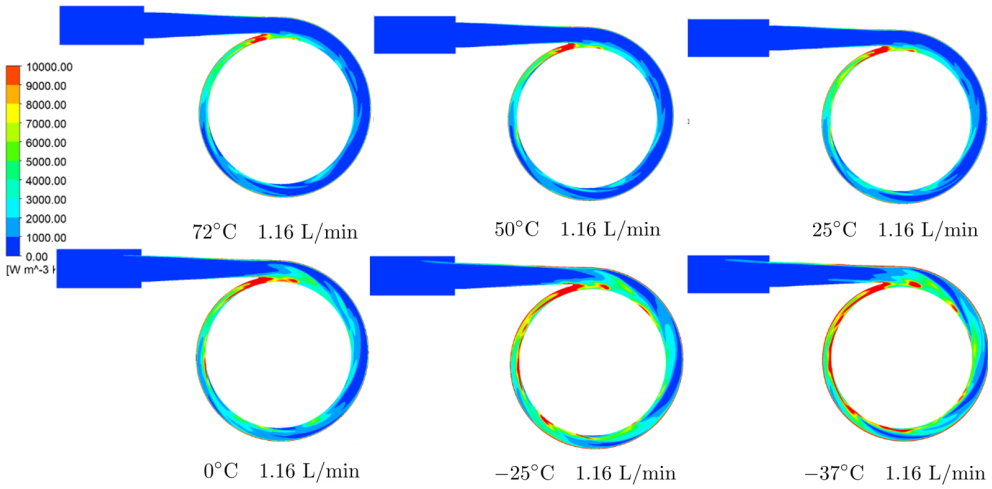


Figure 26. Entropy production rate distribution contour of the volute mid-axial section at 8000 rpm, 1.16 L/min and different temperatures.

The impeller outer edge represents the single largest contributor to the total entropy production across the entire operating envelope. This behavior stems from the narrow tip clearance and high peripheral velocity, which generate an intense shear layer where viscous dissipation dominates. Low-temperature operation exacerbates this condition by raising the fluid viscosity, thereby amplifying frictional dissipation and elevating the local EPR. Moreover, the outer-edge flow structure exhibits considerable geometric sensitivity: small perturbations in the tip clearance induce disproportionately large disturbances in the near-wall velocity field, promoting additional mixing losses. This clearance-induced dissipation enhancement is particularly severe at low temperatures, indicating that thermal conditions and tip-clearance tolerances are coupled determinants of the overall loss budget—a finding with direct implications for the mechanical design of micropumps intended for wide-temperature-range orbital service.

The entropy production rate at the impeller outer edge is highest at low temperatures and decreases monotonically with increasing temperature, and its contribution always dominates. The difference in entropy production rates between the long and short blades is mainly determined by geometric characteristics and flow separation intensity, but their overall contribution is lower than that of the impeller outer edge.

Figure 28 displays upper shroud wall entropy production rate distribution contour at rated flow rate and different temperatures. Through observation of the total wall entropy production rate distribution on the upper shroud, with the change in temperature, the entropy production rates at the impeller outer edge and the blade gap wall show different trends. At the impeller outer edge, regardless of the temperature, the entropy production rate is relatively high, especially at low temperatures, such as at −37 °C, where the entropy production rate at the impeller outer edge is significantly higher than at other positions. As the temperature gradually increases, although the entropy production rate decreases somewhat, it remains at a relatively high level compared to other positions. For the long

and short blade sections, at low temperatures, the high fluid viscosity leads to significant friction losses and high entropy production rates, but as the temperature increases, the viscosity decreases, friction losses are reduced, and the entropy production rate gradually decreases. The long and short blades gap with the upper shroud at low temperatures, due to friction, the entropy production rate is also relatively high, but overall, the entropy production rate at the impeller outer edge always dominates.

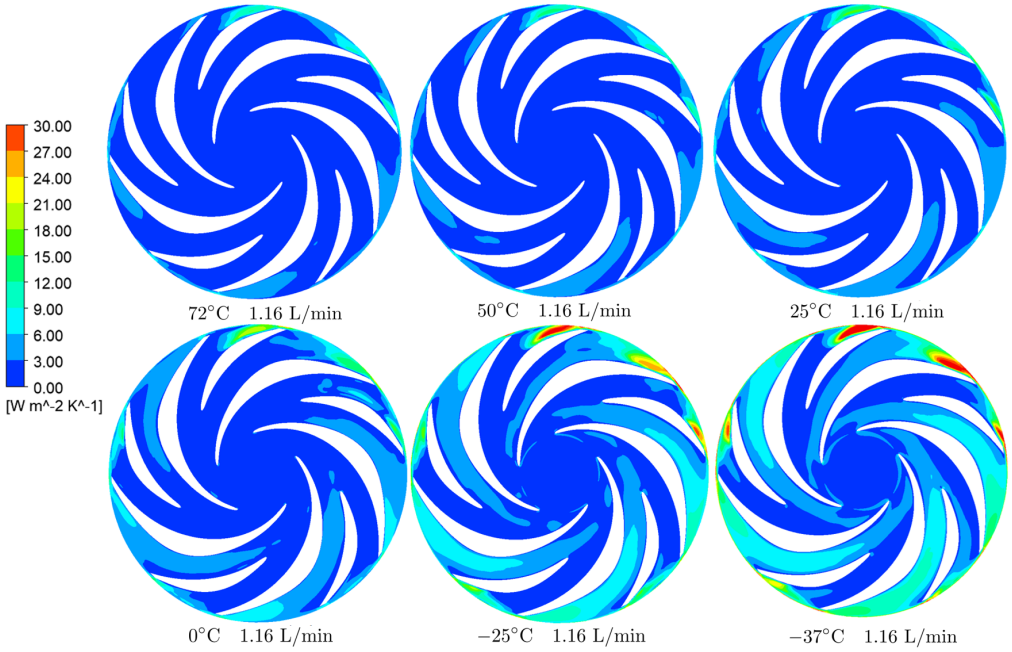


Figure 27. Entropy production rate distribution contour of the lower shroud wall at 8000 rpm, 1.16 L/min and different temperatures.

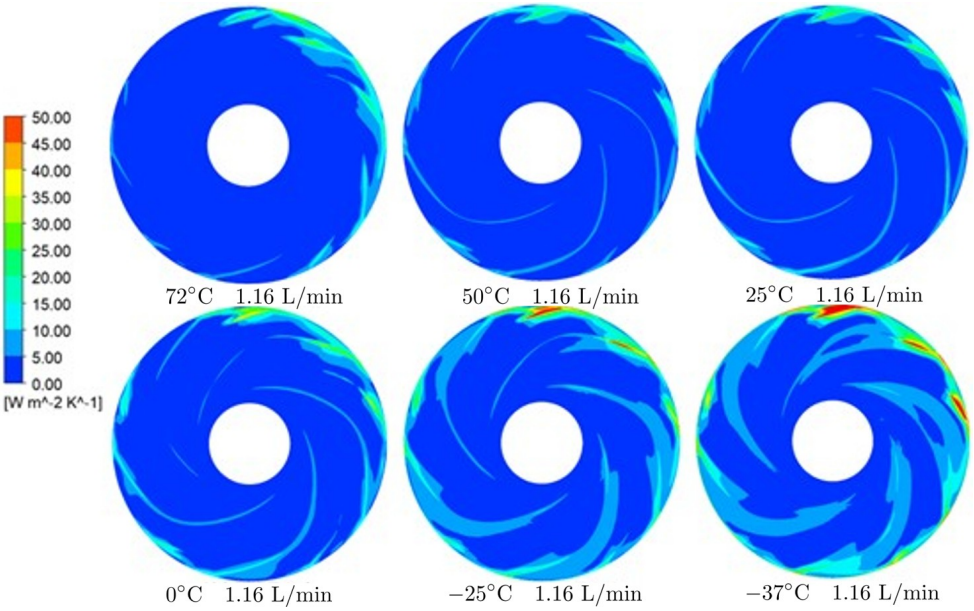


Figure 28. Entropy production rate distribution contour of the upper shroud wall at 8000 rpm, 1.16 L/min and different temperatures.

Figure 29 presents the entropy production rate (EPR) contours on the mid-axial section of the impeller region at −37 °C and 72 °C across a range of flow rates. At the hub region, the EPR remains consistently low across all thermal and flow conditions, indicating negligible local dissipative losses—a consequence of the relatively low velocity gradients

and reduced shear activity near the hub. As the flow rate increases from 0.5 to 2.0 L/min, a marginal EPR rise is observable at the hub, albeit remaining at a substantially low baseline. On the pressure-side leading-edge regions of both the long and short blades, the EPR exhibits a pronounced positive correlation with flow rate, suggesting intensified shear and incipient losses at higher through-flow velocities. In the impeller outer-edge zone, the EPR is uniformly high across all temperatures and flow rates, with particularly elevated values under high-flow-rate conditions, reaffirming this region as the dominant source of entropy generation within the impeller.

Comparing the entropy production rate distributions at different flow rates, it can be found that the increase in flow rate leads to a significant increase in the entropy production rate inside the impeller, especially at the inlet edge working surfaces of the long and short blades and in the impeller outer edge region. This may be because at higher flow rates, the increased fluid velocity leads to greater pressure losses and turbulence, thereby increasing the entropy production rate.

The entropy production rate is governed by a combination of hydrodynamic and thermal factors. Increasing flow rate elevates the through-flow velocity, which in turn intensifies pressure losses and turbulent fluctuations, thereby promoting entropy generation. Regarding thermal effects, the relationship is more nuanced: although elevated temperature reduces viscosity and enhances fluidity, it does not necessarily lead to higher EPR. Instead, the diminished viscous dissipation at higher temperatures tends to suppress the frictional component of entropy production, while any potential increase in flow complexity—if present—is secondary to the viscosity-mediated loss reduction observed in the present study.

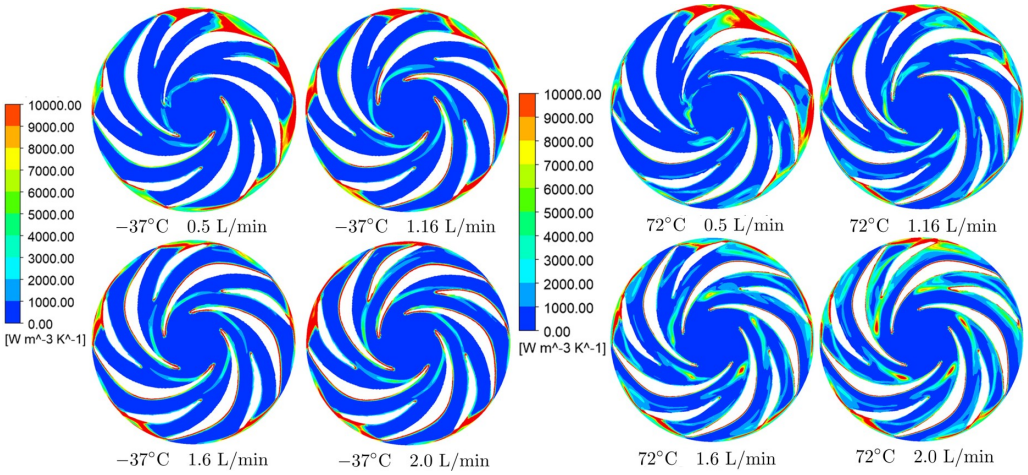


Figure 29. Different flow rates −37 °C and 72 °C impeller mid-axial section entropy production rate distribution contour.

Figure 30 presents the space micropump at −37 °C and 72 °C and at different flow rates in the volute region mid-axial section entropy production rate distribution contour. Due to the change in flow direction near the volute tongue, the entropy production rate in this region is generally high. At small flow rates, the fluid velocity is low, and the fluid energy is mainly converted through local flow disturbances. The flow may exhibit large vortices. At low temperature (−37 °C), due to the high fluid viscosity, the turbulence phenomenon intensifies, and consequently the entropy production rate near the tongue increases significantly. At high temperature (72 °C), the fluid viscosity is lower, the flow is more stable, and therefore the entropy production rate at this position is lower. At large flow rates, the flow velocity increases, local vortices and disturbances decrease, the fluid flow in the tongue region tends to be stable, and the entropy production rate decreases significantly.

At low temperatures, due to the high fluid viscosity, certain turbulence phenomena may still exist in the flow, resulting in a slightly higher entropy production rate at this position than under high-temperature conditions. At high temperatures, the flow is more stable and the entropy production rate is lower.

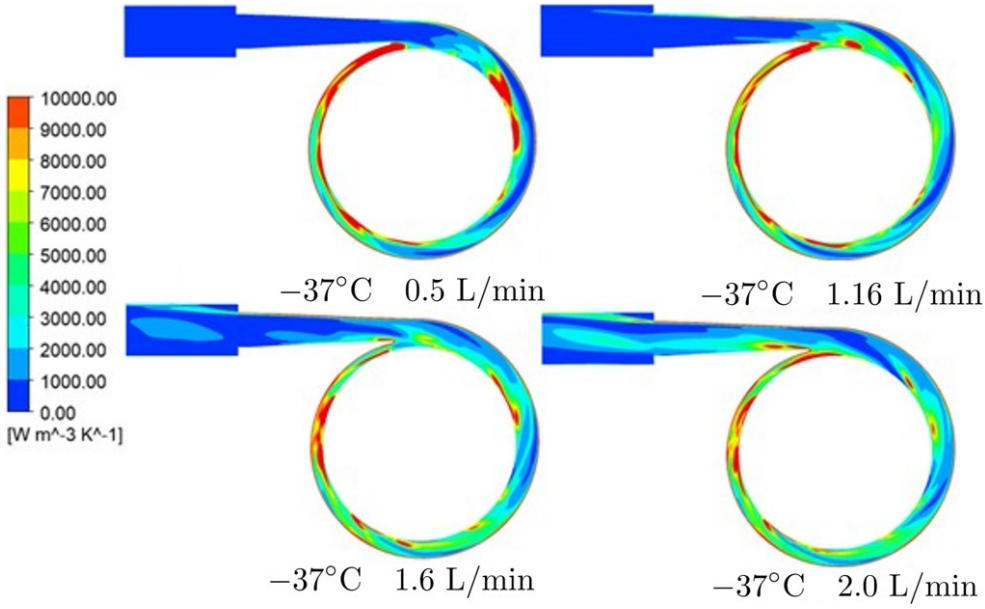
For the volute flow channel at the impeller outer edge, at small flow rates, the fluid velocity is low, and flow separation and turbulence are prone to occur, leading to a high entropy production rate in this region. Especially at low temperature (−37 °C), the high fluid viscosity increases the flow resistance and enhances local vortices, so the entropy production rate at this position increases significantly. In contrast, at high temperature (72 °C), the low fluid viscosity makes the flow smoother, reduces turbulence phenomena, and results in a lower entropy production rate. As the flow rate increases, the fluid velocity increases, turbulence phenomena weaken, the flow becomes more stable, and the entropy production rate at this position decreases.

The region near the volute outer wall is the final region of fluid flow inside the volute, where the fluid velocity and pressure change significantly, resulting in a relatively high entropy production rate in this region. At small flow rates, the low fluid velocity and insufficient fluid kinetic energy are prone to generating strong vortices and turbulence, thereby increasing energy losses and entropy production rates. Especially at low temperature (−37 °C), the increased fluid viscosity enhances vortices, and significantly increases the entropy production rate in this region. At high temperatures, the flow is more stable with fewer vortices, and the entropy production rate is relatively low. Under large flow rate conditions, the increased fluid velocity reduces vortices and turbulence phenomena, resulting in decreased entropy production rates.

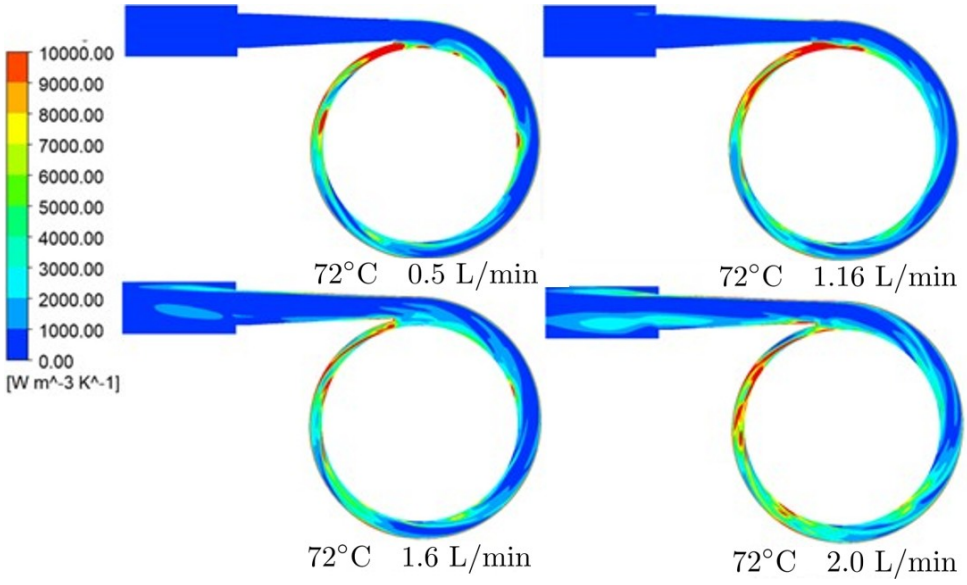
Figure 31 demonstrates the space micropump at −37 °C and 72 °C and lower shroud wall entropy production rate distribution contour at different flow rates. Under low-temperature (−37 °C) conditions, as the flow rate increases, the entropy production rates in the working surface and back surface regions of both the long and short blades show an overall upward trend, especially at a flow rate of 2.0 L/min, where the entropy production rate in the blade region is significantly higher than at other flow rates. This is because at low temperatures, the high fluid viscosity leads to intensified friction losses between the fluid and the blades as the flow rate increases, resulting in increased entropy production rates. Meanwhile, the entropy production rate at the impeller outer edge is also high at low temperatures and increases with the flow rate, but its increase is relatively smaller compared to the blade region.

Under high-temperature operation (72 °C), the overall EPR level is substantially lower than that observed at cryogenic conditions. This reduction is primarily attributable to the temperature-induced decrease in fluid viscosity, which attenuates the wall shear stresses and internal friction losses that constitute the dominant dissipation mechanisms within the micropump. The resulting suppression of viscous dissipation effectively curtails the irreversible loss generation across the entire flow domain.

A comprehensive comparison of the EPR distributions across all tested temperatures and flow rates reveals that the impeller outer edge consistently contributes the largest share to the total wall entropy production on the lower shroud. This dominance is attributed to the peak tangential velocity at the blade periphery, which, in conjunction with the adjacent volute wall, sustains an intense shear layer wherein viscous dissipation prevails as the primary loss mechanism.



(**a**) −37 °C



(**b**) 72 °C

Figure 30. Different flow rates −37 °C and 72 °C volute mid-axial section entropy production rate distribution contour.

Figure 32 presents the EPR distributions on the upper shroud wall of the space micropump at −37 °C and 72 °C under varying flow rates. At cryogenic conditions (−37 °C), the EPR in the blade–shroud clearance regions increases markedly with flow rate. This behavior is governed by the elevated fluid viscosity at low temperatures, which amplifies the frictional resistance within the confined clearances as through-flow velocity rises—thereby intensifying viscous dissipation and elevating the local EPR. The impeller outer-edge wall also exhibits a high baseline EPR that increases with flow rate; however, its growth rate is comparatively moderate relative to that observed in the blade–shroud gap zones, indicating a weaker sensitivity to flow-rate variations.

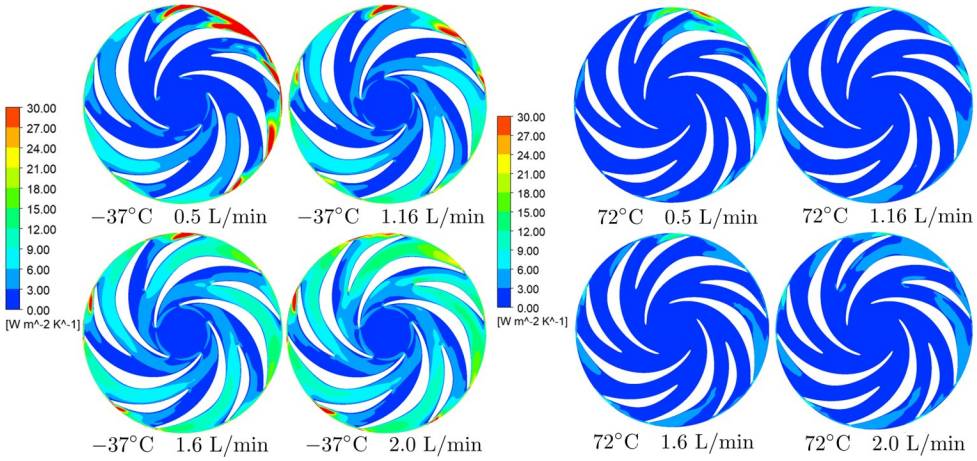


Figure 31. Different flow rates −37 °C and 72 °C lower shroud wall entropy production rate distribution contour.

At elevated temperatures (72 °C), the overall EPR level is substantially reduced compared to the cryogenic baseline. In the blade–shroud clearance regions, the EPR still exhibits an upward trend with increasing flow rate; however, the rate of increase is considerably more moderate than that observed at low temperatures, as the reduced viscosity at high temperatures attenuates the frictional losses within the confined gaps. The impeller outer-edge wall also shows a flow-rate-dependent EPR rise under high-temperature conditions. Notably, across all flow rates, the EPR at the outer-edge wall consistently exceeds that in the clearance regions—a reversal of the relative dominance observed at low temperatures, where the clearance zones exhibited stronger flow-rate sensitivity.

Synthesis of the EPR distributions across the entire parametric space confirms that the impeller periphery consistently experiences the most intense shear interaction with the volute wall, rendering viscous dissipation the dominant loss mechanism regardless of thermal or flow conditions. Consequently, the EPR at the outer-edge wall surpasses that in the blade–shroud clearance zones at every operating point—a finding that complements the preceding observation that while the clearance regions exhibit stronger flow-rate sensitivity at low temperatures, the peripheral zone remains the overarching entropy source across the full spectrum of conditions.

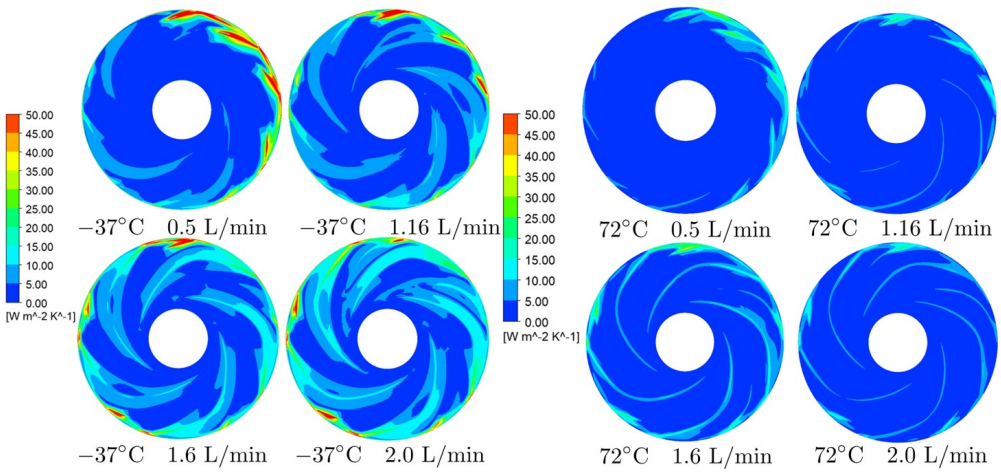


Figure 32. Different flow rates −37 °C and 72 °C upper shroud wall entropy production rate distribution contour.

4. Conclusions

This paper investigates the space micropump over a wide temperature range (−37 °C to 72 °C), systematically studying its flow characteristics through numerical simulation, and draws the following main conclusions:

(1) The pump's hydraulic performance is governed primarily by the thermal sensitivity of the working fluid's viscosity. Under rated operating conditions, compared with the high temperature condition of 72 °C, the low temperature condition of −37 °C results in a head drop of 5.37%, a shaft power increase of 25.76%, and an efficiency decrease of 10.15%. In particular, below approximately 0 °C, as temperature falls, viscosity increases rapidly, leading to a corresponding growth in internal friction, which manifests as simultaneous reductions in head and efficiency and an increase in shaft power. Above this thermal threshold, the viscosity–temperature curve flattens, and the performance metrics change more slowly.

(2) Temperature has a significant influence on the pressure distribution, streamline patterns, and turbulent kinetic energy distribution in the impeller and volute. Under low-temperature conditions, the increased fluid viscosity leads to an expanded high-pressure region and increased static pressure in the impeller region, but the maximum turbulent kinetic energy decreases. Near the volute tongue, where the pressure gradient and velocity gradient are maximum, the turbulent kinetic energy reaches its peak and decreases with decreasing temperature.

(3) Analysis based on the entropy production theory indicates that the volute is the component with the most severe energy loss in the micropump, accounting for over 34% of the total, followed by the blade and shroud regions. The impeller periphery emerges as the dominant dissipation zone across the full temperature envelope, with the intense shear generated at the blade-tip/volute interface accounting for the largest single contribution to the pump's entropy production budget. Under low-temperature conditions, the entropy production losses in each region increase significantly, and the high entropy production regions expand from locally isolated distributions at high temperatures to continuous large-scale distributions at low temperatures, reflecting a transition in the energy loss mechanism.

(4) Within the studied flow rate range, the energy loss of the micropump is minimum at the rated flow rate, and deviation from the rated flow rate leads to significantly increased flow losses. Under large flow rate conditions, the entropy production rates at the blade inlet edge working surfaces and the impeller outer edge region increase significantly; under small flow rate conditions, strong vortices are generated near the volute tongue due to flow turning, resulting in significantly increased entropy production rates.

In summary, medium temperature exerts a pronounced influence on both the hydrodynamic characteristics and the irreversible loss distribution of the space micropump, with fluid viscosity being the primary mediating physical property. The present findings map the temperature-dependent evolution of internal flow topology and the associated energy dissipation pathways, establishing a physically grounded basis for designing micropumps that maintain robust performance across the demanding thermal envelope of orbital applications.

Furthermore, to improve computational efficiency without compromising macroscopic accuracy, the MRF-based steady-state simulation is adopted in the present study. However, this approach is currently unable to resolve the actual unsteady flow phenomena in the vicinity of high-loss regions such as the volute tongue. In future work, transient simulations will be considered to enable a more in-depth investigation and discussion of these regions.

https://doi.org/10.3390/aerospace13080674

Author Contributions: Conceptualization, D.Z.; methodology, D.Z., J.L. and Z.Q.; software, L.M., Z.Q. and K.G.; validation, L.M., Z.Q. and Z.Z.; formal analysis, J.L.; investigation, J.L., Z.Q. and Z.Z.; resources, D.Z.; data curation, J.L.; writing—original draft preparation, D.Z.; writing—review and editing, D.Z. and J.L.; visualization, L.M. and K.G.; supervision, J.L.; project administration, D.Z. and J.L.; funding acquisition, J.L. All authors have read and agreed to the published version of the manuscript.

Funding: This work was supported by the National Natural Science Foundation of China (Grant No. 52176034).

Data Availability Statement: All data generated or analyzed during this study are contained within the published article. Additional requests for data should be addressed to the corresponding author.

Acknowledgments: The authors gratefully acknowledge the reviewers and editors for their valuable comments and suggestions on this manuscript.

Conflicts of Interest: The authors declare that they have no known competing financial interests or personal relationships that could have appeared to influence the work reported in this paper.

References

1. Paris, A.D.; Bhandari, P.; Birur, G.C. High Temperature Mechanically Pumped Fluid Loop for Space Applications—Working Fluid Selection. In Proceedings of the SAE Technical Paper Series, Warrendale, PA, USA, 19 July 2004. [CrossRef]
2. Daimaru, T.; Furst, B.; Cappucci, S.; Sunada, E.; Birur, G. Development of an Evaporator Using Porous Wick Structure for a Two-Phase Mechanically Pumped Fluid Loop. In Proceedings of the 49th International Conference on Environmental Systems, Boston, MA, USA, 7–11 July 2019.
3. Valdarno, L.; Dhir, V.; Furst, B.; Sunada, E. Heat Transfer Modeling in the Wick Structure of an Innovative Evaporator for a Two-Phase Mechanically Pumped Loop. In Proceedings of the 2020 International Conference on Environmental Systems, Sydney, Australia, 3–5 December 2020.
4. Lv, Y.G.; Wang, Y.T.; Meng, T.; Wang, Q.W.; Chu, W.X. Review on Thermal Management Technologies for Electronics in Spacecraft Environment. *Energy Storage Sav.* **2024**, *3*, 153–189. [CrossRef]
5. Neumaier, R. *Hermetic Pumps: The Latest Innovations and Industrial Applications of Sealless Pumps*; Gulf Professional Publishing: Woburn, MA, USA, 1997. [CrossRef]
6. Cheng, W.; Shao, C.; Fan, H. Impacts of Cavitation on Flow Field Distributions and Pump Stability in Cryogenic Pumps. *J. Low Temp. Phys.* **2023**, *211*, 86–107. [CrossRef]
7. Franc, J.P.; Michel, J.M. *Fundamentals of Cavitation*; Springer: Berlin/Heidelberg, Germany, 2005. [CrossRef]
8. Lu, J.; Yuan, S.; Luo, Y.; Yuan, J.; Zhou, B.; Sun, H. Numerical and Experimental Investigation on the Development of Cavitation in a Centrifugal Pump. *Proc. Inst. Mech. Eng. Part E* **2014**, *230*, 213–214. [CrossRef]
9. Ge, M.; Petkovšek, M.; Zhang, G.; Jacobs, D.; Coutier-Delgosha, O. Cavitation Dynamics and Thermodynamic Effects at Elevated Temperatures in a Small Venturi Channel. *Int. J. Heat Mass Transf.* **2021**, *170*, 120970. [CrossRef]
10. Wu, X.; Liu, Y.; Li, Z.; Yin, X.; Chen, T. Numerical Study of Cavitating Flows in an External Gear Pump with Special Emphasis on Thermodynamic Effects. *Appl. Sci.* **2025**, *15*, 3529. [CrossRef]
11. Friedrichs, J.; Kosyna, G. Rotating Cavitation in a Centrifugal Pump Impeller of Low Specific Speed. *J. Fluids Eng.* **2002**, *124*, 356–362. [CrossRef]
12. Coutier-Delgosha, O.; Fortes-Patella, R.; Reboud, J.L.; Hofmann, M.; Stoffel, B. Experimental and Numerical Studies in a Centrifugal Pump with Two-Dimensional Curved Blades in Cavitating Condition. *J. Fluids Eng.* **2003**, *125*, 970–978. [CrossRef]
13. Rakibuzzaman, M.; Kim, K.; Suh, S.H. Numerical and Experimental Investigation of Cavitation Flows in a Multistage Centrifugal Pump. *J. Mech. Sci. Technol.* **2018**, *32*, 1071–1078. [CrossRef]
14. Dehghan, A.A.; Shojaeefard, M.H.; Roshanaei, M. Exploring a New Criterion to Determine the Onset of Cavitation in Centrifugal Pumps from Energy-Saving Standpoint; Experimental and Numerical Investigation. *Energy* **2024**, *293*, 130681. [CrossRef]
15. Tao, R.; Xiao, R.; Wang, F.; Liu, W. Cavitation Behavior Study in the Pump Mode of a Reversible Pump-Turbine. *Renew. Energy* **2018**, *125*, 655–667. [CrossRef]
16. Zhang, X.; Lai, X.; Liao, J.; Liao, G. Influence of Inlet Diameters of Splitter Blades on the Cavitation Performance of Centrifugal Pumps. *J. Eng. Therm. Energy Power* **2017**, *32*, 45–50. [CrossRef]
17. Sarosdy, L.R.; Acosta, A.J. Note on Observations of Cavitation in Different Fluids. *J. Basic Eng.* **1961**, *83*, 399–400. [CrossRef]
18. Stahl, H.A.; Stepanoff, A.J. Thermodynamic Aspects of Cavitation in Centrifugal Pumps. *J. Fluids Eng.* **1956**, *78*, 1691–1693. [CrossRef]

19. Gelder, T.F.; Moore, R.D.; Ruggeri, R.S. *Cavitation Similarity Considerations Based on Measured Pressure and Temperature Depressions in Cavitated Regions of Freon 114*; Technical Report; NASA: Washington, DC, USA , 1966.
20. Moore, R.D.; Ruggeri, R.S. *Prediction of Thermodynamic Effects of Developed Cavitation Based on Liquid-Hydrogen and Freon-114 Data on Scaled Venturis*; Technical Report; National Aeronautics and Space Administration: Moffett Field, CA, USA, 1968.
21. Moore, R.D.; Ruggeri, R.S. *Method for Prediction of Pump Cavitation Performance for Various Liquids, Liquid Temperatures, and Rotative Speeds*; Technical Report; National Aeronautics and Space Administration: Moffett Field, CA, USA, 1969.
22. Hord, J. *Cavitation in Liquid Cryogens. 3: Ogives*; Technical Report; NASA: Greenbelt, MD, USA, 1973.
23. Franc, J.P.; Janson, E.; Morel, P.; Rebattet, C.; Riondet, M. Visualizations of Leading Edge Cavitation in an Inducer at Different Temperatures. In Proceedings of the 4th International Symposium on Cavitation, Pasadena, CA, USA, 20–23 June 2001.
24. Franc, J.P.; Rebattet, C.; Coulon, A. An Experimental Investigation of Thermal Effects in a Cavitating Inducer. *J. Fluids Eng.* **2004**, *126*, 716–723. [CrossRef]
25. Cervone, A.; Testa, R.; Bramanti, C.; Rapposelli, E.; d'Agostino, L. Thermal Effects on Cavitation Instabilities in Helical Inducers. *J. Propul. Power* **2005**, *21*, 307–326. [CrossRef]
26. Cervone, A.; Bramanti, C.; Rapposelli, E.; D'Agostino, L. Thermal Cavitation Experiments on a NACA 0015 Hydrofoil. *J. Fluids Eng.* **2005**, *128*, 326–331. [CrossRef]
27. Hosien, M.A.; Selim, S.M. Experimental and Theoretical Investigation on the Effect of Pumped Water Temperature on Cavitation Breakdown in Centrifugal Pumps. *J. Appl. Fluid Mech.* **2017**, *10*, 1079–1089. [CrossRef]
28. Shrestha, U.; Kim, D.; Choi, Y.D. Thermodynamic Characteristics of the Hydraulic and Suction Performances by the Working Fluid Temperature of Multistage Centrifugal Pump. *KSFM J. Fluid Mach.* **2023**, *26*, 90–99. [CrossRef]
29. Valdarno, L.; Dhir, V.K.; Furst, B.; Sunada, E. Numerical and Experimental Investigation of Heat Transfer in the Porous Media of an Additively Manufactured Evaporator of a Two-Phase Mechanically Pumped Loop for Space Applications. *Microgravity Sci. Technol.* **2024**, *36*, 40. [CrossRef]
30. Qi, H.; Li, W.; Ji, L.; Liu, M.; Song, R.; Pan, Y.; Yang, Y. Performance Optimization of Centrifugal Pump Based on Particle Swarm Optimization and Entropy Generation Theory. *Front. Energy Res.* **2023**, *10*, 1094717. [CrossRef]
31. Shi, L.; Jiang, Y.; Shi, W.; Sun, Y.; Qiao, F.; Tang, F.; Xu, T. Numerical Analysis of Energy Loss in Stall Zone for Full Tubular Pump Based on Entropy Generation Theory. *J. Mar. Sci. Eng.* **2023**, *11*, 895. [CrossRef]
32. Gong, R.; Wang, H.; Chen, L.; Li, D.; Zhang, H.; Wei, X. Energy Loss Analysis in Hydraulic Turbine Based on Entropy Generation Theory. *Sci. China Technol. Sci.* **2013**, *25*, 622–630. [CrossRef]
33. Bhandari, P.; Birur, G.; Ganapathi, G.; Paris, A.;Pauken, M.; Novak, K.; Tsuyuki, G. Mechanically Pumped Fluid Loops for Spacecraft Thermal Control: Past, Present & Future. In Proceedings of the 15th Annual Thermal & Fluid Analysis Workshop, Pasadena, CA, USA, 3 September 2004.
34. Birur, G.C.; Waniewski Sur, T.; Paris, A.D.; Shakkottai, P.; Green, A.A.; Haapanen, S.I. Micro/Nano Spacecraft Thermal Control Using a MEMS-Based Pumped Liquid Cooling System. In *Microfluidics and BioMEMS*; SPIE: Cergy-Pontoise, France, 2001; Volume 4560, pp. 196–206. [CrossRef]
35. Ramadhan Al-Obaidi, A. Effects of Different Turbulence Models on Three-Dimensional Unsteady Cavitating Flows in the Centrifugal Pump and Performance Prediction. *Int. J. Nonlinear Sci. Numer. Simul.* **2019**, *20*, 487–509. [CrossRef]
36. Zhou, J.; Xing, G.; Zhou, S. Effects of Different Turbulence Models on Simulation Accuracy of the Miniature Super-low Specific Speed Centrifugal Pump. In *IOP Conference Series: Materials Science and Engineering*; IOP Publishing: Bristol, UK, 2019; Volume 490, p. 052026. [CrossRef]

Disclaimer/Publisher's Note: The statements, opinions and data contained in all publications are solely those of the individual author(s) and contributor(s) and not of MDPI and/or the editor(s). MDPI and/or the editor(s) disclaim responsibility for any injury to people or property resulting from any ideas, methods, instructions or products referred to in the content.